

Unusual *Hemiaulus* Bloom Influences Ocean Productivity in Northeast U.S. Shelf Waters

S. Alejandra Castillo Cieza¹, Rachel H.R. Stanley^{1*}, Pierre Marrec², Diana N. Fontaine², E. Taylor Crockford³, Dennis J. McGillicuddy Jr.³, Arshia Mehta¹, Susanne Menden-Deuer², Emily E. Peacock³, Tatiana A. Rynearson², Zoe O. Sandwith^{3,4}, Weifeng (Gordon) Zhang³, and Heidi M. Sosik³

¹Chemistry Department, Wellesley College, Wellesley, 02481, USA

²Graduate School of Oceanography, University of Rhode Island, Narragansett, 02882, USA

³Woods Hole Oceanographic Institution, Woods Hole, MA, 02543, USA

⁴Now at the Hakai Institute, Pruth Harbour, Calvert Island, BC, Canada

*Correspondence to: Rachel H. R. Stanley (rachel.stanley@wellesley.edu)

Abstract. Because of its temperate location, high dynamic range of environmental conditions, and extensive human activity, the long-term ecological research site in the coastal Northeastern U.S. Shelf (NES) of the Northwestern Atlantic Ocean offers an ideal opportunity to understand how productivity shifts in response to changes in planktonic community composition. Ocean production and trophic transfer rates, including Net Community Production (NCP), Net Primary Production (NPP), Gross Oxygen Production (GOP), and microzooplankton grazing rates are key metrics for understanding marine ecosystem dynamics and associated impacts on biogeochemical cycles. Although small phytoplankton usually dominate phytoplankton community composition and Chl-a concentration in the NES waters during the summer, in August 2019, a bloom of the large diatom genus *Hemiaulus*, with N₂ fixing symbionts, was observed in the mid-shelf region. NCP was 2.5 to 9 times higher when *Hemiaulus* dominated phytoplankton carbon compared to NCP throughout the same geographic area during the summers of 2020–2022. The *Hemiaulus* bloom in summer 2019 also coincided with higher trophic transfer efficiency from phytoplankton to microzooplankton, higher GOP and NPP, than in the summers 2020–2022. This study suggests that the dominance of an atypical phytoplankton community that alters the typical size distribution of primary producers can significantly influence productivity and trophic transfer, highlighting the dynamic nature of the coastal ocean. Notably, summer 2018 NCP levels were also high although the size distribution of Chl-a was typical and an atypical phytoplankton community was not observed. A better understanding of the dynamics of the NES in terms of biological productivity is of primary importance, especially in the context of changing environmental conditions due to climate processes.

1 Introduction

Oceans regulate atmospheric carbon dioxide (CO₂) concentrations and support life on Earth via several mechanisms (Friedlingstein et al., 2022). One of these mechanisms is the biological pump, which involves biological, physical, and chemical processes that aid in transporting and sequestering organic carbon from CO₂ (Boyd et al., 2019). As the main primary producers in the ocean, phytoplankton play a major role in the biological pump (Field et al., 1998). Diatoms, a type of photosynthetic algae, are believed to account for nearly half of net marine primary productivity globally and are important contributors to the biological pump (Jin et al., 2006). Diatoms characteristically thrive in nutrient-rich surface layers and turbulent conditions, and are thus typically found at high latitudes and in coastal upwelling regions (Armbrust, 2009). However, new technology (e.g., molecular biology and imaging) has revealed that diatoms may be more prevalent in low nutrient, oligotrophic systems than traditionally considered (Malviya et al., 2016), likely due to unique metabolic capabilities involving nutrient acquisition strategies that enable their survival in low nutrient regimes (Margalef, 1978).

One specific metabolic capability within diatoms is the ability to form a symbiosis with nitrogen-fixing cyanobacteria. This symbiosis, known as a diatom-diazotroph association, has been observed around the globe, mostly in oligotrophic regions (Foster and Zehr, 2019), but also in temperate continental shelf waters (Wang et al., 2021). Furthermore, some diatom-diazotroph associations have the capability to grow very quickly, forming localized

46 blooms (Villareal et al., 2011). Diatom-diazotroph blooms, specifically involving the diatom genus *Hemiaulus* and
47 the symbiont *Richelia*, have been found in warm, stratified waters in various regions around the globe and have been
48 associated with high carbon export observed via a combination of modern oceanographic measurements and paleo-
49 flux case studies. Examples include blooms in the eastern Equatorial Atlantic (Foster and Zehr, 2006), tropical North
50 Atlantic (Carpenter et al., 1999; Subramaniam et al., 2008), North Pacific Subtropical Gyre (Dore et al., 2008;
51 Villareal et al., 2011), and South China Sea (Grosse et al., 2010). Furthermore, at the ALOHA site in the Pacific
52 Ocean north of Hawaii, blooms of the *Hemiaulus-Richelia* association can last as long as 30 days and contribute
53 significantly (20%) to annual carbon flux in this region (Kemp and Villareal, 2018; Karl et al., 2012). Diatoms with
54 nitrogen-fixing symbionts are thus important contributors to primary productivity and carbon export, especially at
55 times when surface waters are depleted of dissolved inorganic nitrogen (Tang et al., 2020).

56 An intense bloom of *Hemiaulus* and its symbiont *Richelia* was observed in summer 2019 in temperate
57 Northeast U.S. Shelf (NES) surface waters. The NES region in the Northwestern Atlantic Ocean is particularly
58 productive, favoring enhanced inorganic carbon sequestration by the biological pump, and supports an ecologically
59 and economically important ecosystem (Townsend et al., 2006). Like other marine regions, the NES food web is
60 fueled by phytoplankton, the main primary producers, which play a fundamental role in the ecosystem (e.g. Mouw
61 and Yoder, 2005; O'reilly and Zetlin, 1998; Yoder et al., 2002). Productivity is heavily influenced by abiotic factors
62 in the NES region. For instance, strong seasonal variations in water temperature, stratification and cross-shelf
63 advection on the NES affect nutrient supply and lead to seasonal shifts in phytoplankton productivity and species
64 composition (Li et al., 2015; Oliver et al., 2022; Zhang et al., 2023). Furthermore, the water temperature of the NES
65 is rising faster than the global average (Chen et al., 2020; Karmalkar and Horton, 2021; Shearman and Lentz, 2010),
66 leading to unknown consequences for phytoplankton community composition and productivity within this important
67 and dynamic coastal region.

68 To further understand phytoplankton population dynamics and their influence on the ocean's biological
69 pump, the NES Long-Term Ecological Research (NES-LTER, <https://nes-lter.whoi.edu/>) project investigates
70 primary productivity, food web structure and ecosystem dynamics with a focus on southern New England coastal
71 waters. As part of the NES-LTER project, phytoplankton and zooplankton community composition, phytoplankton
72 growth rates, microzooplankton grazing rates, and productivity rates are determined on week-long research cruises
73 which have occurred quarter-annually since 2018. To quantify productivity, several different rates are estimated
74 from data collected on these cruises, including Gross Oxygen Production (GOP), Net Primary Production (NPP),
75 Net Community Production (NCP) and export efficiency ratios (NCP/GOP). GOP is similar to Gross Primary
76 Production; it represents total photosynthesis in oxygen units and also includes photoprocesses that produce oxygen
77 (Juraneck and Quay, 2013). NPP is photosynthetic production minus autotrophic respiration and thus represents the
78 net production activity of the phytoplankton community. NCP is the balance of photosynthesis and community
79 respiration (autotrophic plus heterotrophic) and is equal, on long enough spatial and temporal scales, to the amount
80 of carbon exported out of the surface of the ocean (Emerson, 2014). The NCP/GOP ratio, analogous to the f-ratio
81 (Dugdale and Goering, 1967), is indicative of export efficiency, with a high ratio implying that the community is
82 exporting most of the carbon (organic matter) produced and thus recycling only a little (Juraneck and Quay, 2013).

83 The composition and size structure of the phytoplankton community in the NES-LTER study are
84 investigated concurrently from automated imaging and size-fractionated chlorophyll-a (Chl-a). In winter, the NES
85 waters tend to be nutrient-rich due to enhanced vertical mixing and input of river and estuary waters that promote
86 high levels of surface Chl-a, with a dominance of large phytoplankton cells that grow slowly (Marrec et al., 2021).
87 Conversely, during a typical summer, nutrients become depleted in the surface mixed layer, leading to low Chl-a
88 concentrations dominated by fast-growing small phytoplankton cells (Marrec et al., 2021; O'reilly and Zetlin,
89 1998).

90 To complement production estimates and phytoplankton community structure observations, the flow of
91 carbon from primary producers to higher trophic levels on the NES has also been investigated. Microzooplankton,
92 protists smaller than 200 μm , are a crucial link between primary producers and higher trophic levels because they
93 often consume 60–70% of daily primary production (Landry and Calbet, 2004; Schmoker et al., 2013). In the NES,
94 while phytoplankton grow faster during the summer than in winter, microzooplankton grazing rates tend to stay
95 relatively constant across seasons (Marrec et al., 2021). Thus, during winter, phytoplankton growth rates and
96 microzooplankton grazing rates are typically well coupled and show a close 1:1 ratio, with microzooplankton
97 consuming most of the primary production (Marrec et al., 2021). During the summer, phytoplankton growth and
98 microzooplankton grazing rates are typically decoupled, leading to less than 50% of the primary production
99 consumed by microzooplankton. The degree of coupling between microzooplankton grazing and phytoplankton
100 growth rates is associated with phytoplankton size structure (Marrec et al., 2021) and likely species composition,

101 and is an important indicator of the trophic transfer efficiency from phytoplankton to microzooplankton at the base
102 of the planktonic food web.

103 Here, we examined the association between productivity, phytoplankton composition and
104 microzooplankton grazing, key components of trophic transfer efficiency and ecosystem function. During a NES-
105 LTER cruise in summer 2019, we observed an anomalous relationship between growth and grazing rates, as well as
106 dramatically different productivity rates and community composition compared to other summer cruises in the NES
107 region. We thus investigated how a diatom bloom of *Hemiaulus*, with diazotrophic symbionts, affected metrics of
108 productivity and grazing on the NES during the summer of 2019. Our results provide insights into the effects of
109 community composition on productivity rates.

110 2 Methods

111 Measurements of environmental conditions, chemical and biological stocks, and productivity and grazing rates were
112 conducted on multiple cruises within the framework of the NES-LTER program (Table 1). Measurements from three
113 other cruises from different projects on the NES were also included in this analysis for comparison (project names in
114 Table 1) and *Hemiaulus* abundances were further compared to an additional 26 cruises in the NES (Table S1). From
115 the time series, we were able to better understand an event that was observed on the 2019 NES-LTER summer
116 cruise (EN644) which occurred August 20 to 25 (Table 1). Some data during that event, such as surface seawater
117 temperature (SST), salinity (SSS), NCP rates, and phytoplankton composition were collected continuously from the
118 underway system (every 0.1 to 6 km depending on the measurement type and ship speed), while other parameters
119 (e.g., NPP, grazing rates, Chl-a, nutrients) were measured discretely at the NES-LTER stations (Fig. 1, Table S2).
120 Main stations were located with ~ 19 km spacing on a north-to-south transect primarily along 70.883° W. Fig. 1
121 shows the cruise track for the August 2019 NES-LTER cruise, but all the other NES-LTER cruises had a near
122 identical cruise track. In particular, the mid-shelf region, which is where the *Hemiaulus* bloom primarily occurred,
123 corresponds to 50 – 100 m water depth and was bounded by latitudes 40.980 °N to 40.327 °N. The mid-shelf region
124 contains four stations. Exact locations and dates of when the mid-shelf stations were occupied is provided in Table
125 S2.

126 At each station, water was collected via Niskin bottles mounted on a CTD-rosette (conductivity-
127 temperature-depth, Seabird SBE32 Carousel Water Sampler). The CTD-rosette system consisted of a 24-bottle
128 rosette frame with 10-L Niskin bottles. Depth, temperature, and salinity were collected with a SBE911 CTD
129 (Seabird Electronics) equipped with additional sensors for chlorophyll fluorescence (WET Labs ECO-AFL/FL),
130 photosynthetically active radiation (PAR, Biospherical Instruments® QSP2000), and beam attenuation (WET Labs
131 C-Star 25-cm transmissometer). The Niskin bottles were closed at various depths ranging from surface to near
132 bottom, based on the depths of the mixed layer, euphotic zone, and Chl-a maximum. Mixed layer depths were
133 calculated from the temperature and salinity data from the CTD with the threshold method where the mixed layer
134 was taken to be the depth where the density difference between the surface and bottom of the mixed layer was
135 greater than $\Delta\sigma_\theta = 0.125 \text{ kg m}^{-3}$ (De Boyer Montegut et al., 2004). Mixed layer depths were confirmed to be similar
136 when a gradient criterion with a difference of 0.0125 kg m^{-3} was used instead (Kara et al., 2000). Euphotic Zone was
137 taken to be the depth at which light was 1% of the surface value. Chl-a max was chosen based on the depth with
138 maximum fluorescence observed in the CTD cast. Water from the Niskins was used to quantify a number of
139 parameters as described in Sections 2.2 through 2.5.

140 The underway system consisted of continuous surface seawater pumped throughout the ship by an impeller pump
141 and a diaphragm pump located near the ship's bow. Using water from the impeller pump, continuous measurements
142 of surface temperature and salinity were obtained from a Seabird SBE38 (temperature) sensor installed at the water
143 intake and by a Seabird SBE45 sensor (temperature and salinity) located further away in the underway system.
144 Because the diaphragm pump is less likely to damage plankton (Cetinic et al., 2016), its underway flow was used for
145 measurements to quantify NCP (Section 2.1), GOP (Section 2.2), and phytoplankton community composition
146 (Section 2.8). The ship steamed both south and north along the longitude 70.883°W and thus over the 6-day cruise,
147 the underway data sampled the same locations at multiple points in time. Stations were only occupied at one time
148 per cruise.

149

150

151

152 **Table 1.** Dates of the summer cruises, as well as project and ship names and cruise numbers, that are presented in
 153 this paper. Project name abbreviations are as follows: OTZ– Ocean Twilight Zone, SPIROPA–Shelfbreak
 154 Productivity Interdisciplinary Research Operation at the Pioneer Array (Oliver et al., 2021), and EcoMon–
 155 Ecosystem Monitoring program run by the National Oceanic and Atmospheric Administration. Cruise tracks for the
 156 NES-LTER transects are shown in Fig. 1. The SPIROPA and OTZ cruises followed the same longitude 70.883°W
 157 when in the mid-shelf region and thus data used from those cruises is collocated with the NES-LTER data.

Cruise	Start date/End date	Project name	Ship
EN617	20 July 2018 – 25 July 2018	NES-LTER	<i>R/V Endeavor</i>
TN368	05 July 2019 – 18 July 2019	SPIROPA	<i>R/V Thomas G. Thompson</i>
HB1907	25 July 2019 – 08 Aug 2019	OTZ	<i>NOAA Ship Henry B Bigelow</i>
GU1902	16 Aug 2019 – 29 Aug 2019	EcoMon	<i>NOAA Ship Gordon Gunter</i>
EN644	20 Aug 2019 – 25 Aug 2019	NES-LTER	<i>R/V Endeavor</i>
EN655	25 July 2020 – 28 July 2020	NES-LTER	<i>R/V Endeavor</i>
EN668	16 July 2021 – 21 July 2021	NES-LTER	<i>R/V Endeavor</i>
EN687	29 July 2022 – 03 Aug 2022	NES-LTER	<i>R/V Endeavor</i>

158

159 2.1 Net Community Production

160 Net community production rates were calculated from O₂/Ar ratios measured by an at-sea Equilibrator Inlet
 161 Mass Spectrometer (EIMS) (Cassar et al., 2009) analyzing water from the ship’s underway system and from discrete
 162 samples collected from both CTD Niskin bottles and from the underway system. The EIMS was used to collect
 163 continuous data on O₂/Ar ratios via the diaphragm pump of the underway system that, on the *R/V Endeavor*, pumps
 164 seawater from a depth of 5 m. The underway system seawater flows through a debubbler into a bucket at a constant
 165 rate that allows for continuous overflow for consistent head pressure. Water is then pumped from the bucket at ~1.1
 166 L min⁻¹ by a gear pump through two filters: a bag with a 25-μm pore size, and a 2-layered sock with a 5-μm inner
 167 and 100-μm outer pore size. The gear pump then pushes the water through an equilibrator membrane contactor
 168 cartridge (Liqui-Cel Extra-Flow 2.5x8 model G540). The equilibrated headspace gas from the cartridge is then dried
 169 by flowing through the dessicants Nafion and Drierite and then passed via a fused silica capillary into a Hiden
 170 Residual Gas Analyzer (RGA) (HAL 7) quadrupole mass spectrometer. Details of the equilibration method can be
 171 found in Manning et al. (2016), but in this instance were modified to not use SAES getters as they would have
 172 removed the O₂. The EIMS was operated throughout the whole cruise (starting one hour after the ship left port and
 173 ending a few hours before return to port). To calibrate the mass spectrometer, the capillary was switched to an air
 174 inlet for twenty minutes approximately every six hours as the ratio of O₂/Ar in air is stable and well-known.
 175 Additionally, bottle samples were collected from the underway system at least once per day and were subsequently
 176 measured on an isotope ratio mass spectrometer at Woods Hole Oceanographic Institution (see Section 2.2). These
 177 bottle samples were used to provide additional calibration as necessary—such additional corrections changed the
 178 O₂/Ar ratios by at most 0.67%.

179 The O₂/Ar ratios were then used to calculate NCP (Hendricks et al., 2004; Juranek and Quay, 2005; Stanley
 180 et al., 2010). With data from the EIMS and the bottle samples, the biological oxygen saturation Δ(O₂/Ar) was
 181 calculated via the equation below:

$$182 \quad \Delta \left(\frac{O_2}{Ar} \right) = \frac{\left(\frac{O_2}{Ar} \right)_{smp}}{\left(\frac{O_2}{Ar} \right)_{eq}} - 1 \quad (1)$$

183

184

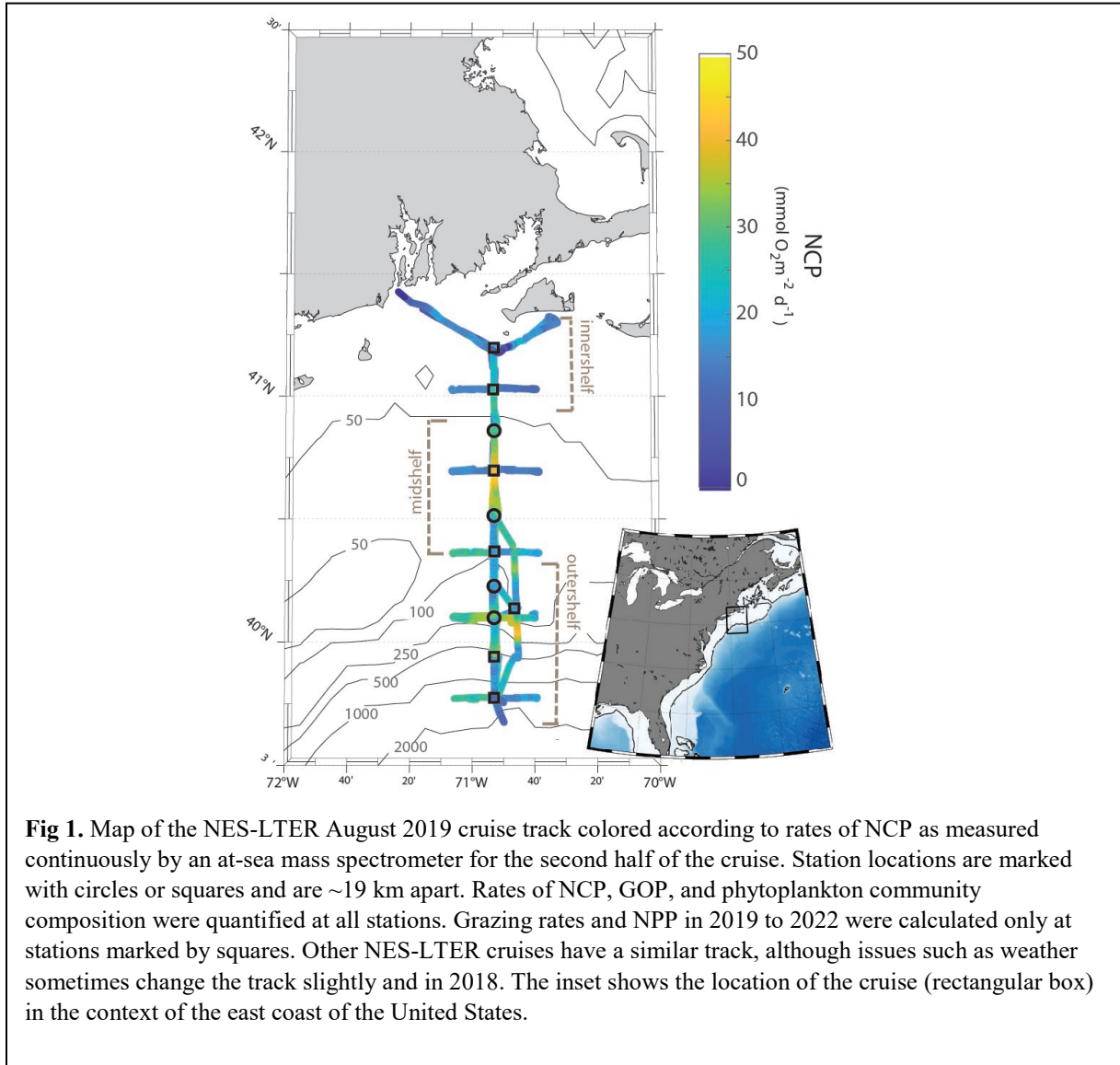


Fig 1. Map of the NES-LTER August 2019 cruise track colored according to rates of NCP as measured continuously by an at-sea mass spectrometer for the second half of the cruise. Station locations are marked with circles or squares and are ~19 km apart. Rates of NCP, GOP, and phytoplankton community composition were quantified at all stations. Grazing rates and NPP in 2019 to 2022 were calculated only at stations marked by squares. Other NES-LTER cruises have a similar track, although issues such as weather sometimes change the track slightly and in 2018. The inset shows the location of the cruise (rectangular box) in the context of the east coast of the United States.

185
186
187
188
189
190
191
192
193
194
195
196
197
198
199
200
201

where $(O_2/Ar)_{\text{smp}}$ represents the ratio of O_2 to Ar ion currents detected by the EIMS after being calibrated with bottle data, and $(O_2/Ar)_{\text{eq}}$ represents the ratio of equilibrium concentrations of the gases determined from the gases' solubility (Garcia and Gordon, 1992; Hamme and Emerson, 2004) at the seawater temperature and salinity.

The NCP integrated over the mixed layer, in units of $\text{mmol } O_2 \text{ m}^{-2} \text{ d}^{-1}$, is calculated as

$$NCP = \Delta \left(\frac{O_2}{Ar} \right) [O_2]_{\text{eq}} k \rho \quad (2)$$

where $[O_2]_{\text{eq}}$ represents the equilibrium concentration of O_2 at the relevant temperature and salinity (mmol kg^{-1}), k is the weighted gas transfer velocity (m d^{-1}), and ρ is the density of seawater (kg m^{-3}) (Millero and Poisson, 1981). The weighted gas transfer velocity is a time-weighted average from over the past 30 days calculated as described in Reuer et al. (2007), with the gas exchange parameterization of Stanley et al., (2009) and wind speeds from NCEP Reanalysis (Kalnay et al., 1996; Kistler et al., 2001). Many physical considerations altering O_2 saturations, such as changes in temperature and bubble injection, do not need to be considered due to the inclusion of Ar which has similar solubility and diffusivity as O_2 ; however, a few assumptions were made for these calculations. Firstly, this equation assumes steady state within the mixed layer, i.e. no change in O_2/Ar in the ocean with time. While O_2/Ar was likely changing in actuality, assuming steady state simply means that the rates calculated reflect an exponentially weighted average of NCP over the past few residence times of oxygen (residence time equals a few days in these conditions) (Teeter et al., 2018). Thus, the assumption of steady state does not majorly impact our

202 conclusions. We were not able to calculate the time rate of change term in O₂/Ar (Manning et al., 2017b) because
 203 the cruise was not Lagrangian, and even though the ship returned to the same geographic location, the water at that
 204 location changed due to ocean currents. To check the assumption that there is negligible respiration within the ship's
 205 lines (Juraneck et al., 2010), bottle samples were collected in duplicate from Niskins at the same time as samples
 206 were collected from the underway system several times during every cruise; gas concentrations in the bottle samples
 207 from the underway and Niskin were identical within measurement errors, confirming there was no detectable
 208 respiration in the ship's line.

209 2.2 Gross Oxygen Production

210 Discrete samples of triple oxygen isotopes (TOI) were collected from the surface Niskin bottles on the CTD-rosette
 211 system at all stations as well as from the underway system between stations. Samples from the CTD-rosette system
 212 were also collected from bottles fired at ~ 5 m below the mixed layer and often one greater depth to provide
 213 information for assessing whether vertical corrections to O₂/Ar ratios were significant. Samples were collected in
 214 custom-made ~500-mL sample bottles which were pre-poisoned with 100 µl of saturated mercuric chloride solution
 215 and filled with around 300 mL of seawater from the underway system or from the Niskin at each station (Stanley et
 216 al., 2015). Samples were brought to Woods Hole Oceanographic Institution where they were analyzed for TOI with
 217 a custom-made processing line and a ThermoFisher MAT 253 isotope ratio mass spectrometer as detailed in Stanley
 218 et al (2015). The same samples were also analyzed for O₂/Ar which yielded rates of NCP from discrete data as well
 219 as an independent method for calibrating the EIMS (see above). Corrections for the effect of argon on the triple
 220 oxygen isotope ratio and the effect of varying sizes of the sample vs. reference standard were made for every
 221 sample. Reproducibility from duplicate samples collected on these cruises ranged from 4 to 8 per meg for ¹⁷Δ, 0.008
 222 to 0.03 per mil for δ¹⁷O, and 0.008 to 0.05 per mil for δ¹⁸O depending on the cruise.

223 From these samples, GOP is calculated in units of mmol O₂ m⁻² d⁻¹ following Prokopenko et al., (2011)
 224 according to:

$$225 \quad \text{GOP} = kO_{\text{eq}} \frac{\frac{x_{\text{dis}}^{17} - x_{\text{eq}}^{17}}{x_{\text{dis}}^{17}} - \lambda \frac{x_{\text{dis}}^{18} - x_{\text{eq}}^{18}}{x_{\text{dis}}^{18}}}{\frac{x_{\text{P}}^{17} - x_{\text{eq}}^{17}}{x_{\text{dis}}^{17}} - \lambda \frac{x_{\text{P}}^{18} - x_{\text{eq}}^{18}}{x_{\text{dis}}^{18}}} \quad (3)$$

226 where *k* again represents the time-weighted gas transfer velocity (m d⁻¹), O_{eq} represents the equilibrium
 227 concentration of oxygen, λ represents the respiration slope factor = 0.5179, X_{dis}* represents the ratio of isotopes
 228 (*O/¹⁶O) dissolved in the sample, X_{eq}* represents the ratio of isotopes (*O/¹⁶O) dissolved in seawater equilibrated
 229 with the atmosphere, and X_P* stands for the ratio of isotopes (*O/¹⁶O) in oxygen that was produced via
 230 photosynthesis. The photosynthetic end member used was the average of the phytoplankton value determined by
 231 Barkan and Luz (2011); Vienna Standard Mean Ocean Water (VSMOW) was used for the isotopic composition of
 232 oxygen in H₂O. The actual isotopic composition of H₂O was measured in a subset of samples to see if corrections
 233 needed to be made (Manning et al., 2017a). It was found to be very similar to VSMOW, leading to an error of less
 234 than 10% in GOP due to isotopic water variations.

235 Confirmation that the water from the underway system was representative of the oceanic TOI signature of
 236 dissolved oxygen was obtained by comparing samples collected from the underway system to those collected
 237 concurrently from the surface Niskin bottle. All cruises, other than 2019, showed that there was statistically no
 238 difference in TOI between water from the underway system and the CTD and thus that the water from the underway
 239 system was representative of the mixed layer at that location and time. During the summer of 2019, the water from
 240 the underway system had TOI values 4.1 per meg lower than that from the CTD – this is within measurement errors
 241 but since it might have led to systematic biases, we corrected for this offset before calculating GOP from the data.
 242 The GOP rates, along with the NCP rates, represent productivity integrated throughout the mixed layer.

243 2.3 Net Primary Productivity

244 Water samples for NPP were collected at 4-7 stations (cruise dependent) from 3-4 depths (station
 245 dependent) from the Niskins on the CTD-rosette system during the summers of 2019 to 2022. During collection,
 246 water was pre-filtered through 200-µm mesh (to remove mesozooplankton) into acid-washed 2-L polycarbonate
 247 bottles. Water collection and associated incubation occurred in triplicate for surface samples at each station. Bottles
 248 were spiked with a solution of 99% NaH¹³CO₃ (Cambridge Isotope Lab, Tewksbury, MA) for a final 10%
 249 enrichment of the dissolved inorganic carbon (DIC) pool and placed in various mesh bags to simulate *in situ* light

250 levels. Bottles were incubated for 24 h in clear deck-board incubators with flowthrough seawater and Onset HOBO
 251 data loggers monitored tank water temperature. At each station, the natural ^{13}C in the water was determined from an
 252 un-spiked sample and dark carbon assimilation was determined from a spiked dark bottle sample. Dark carbon
 253 assimilation was negligible (<1%) so no correction for dark carbon assimilation was applied to this dataset.

254 The corresponding light levels at collection depths were determined using either PAR or beam attenuation
 255 from the CTD cast for each station. When PAR data were not available (e.g., night-time casts), a relationship was
 256 established (eq. 4) with previous daytime cast information between beam attenuation (c , measured by
 257 transmissometer, m^{-1}) and the light extinction coefficient (K_d , m^{-1}) for each cruise. During night-time casts, K_d was
 258 estimated from the average c in the upper 10 m during the cast with the slope (m) and intercept (b) from the daytime
 259 plot, according to equation 4:

$$K_d = (m * At) + b \quad (4)$$

261 The appropriate shading in incubations (%PAR) for each depth of sample collection (z) was estimated as:

$$\%PAR = 100e^{-K_d \times z} \quad (5)$$

264 At the end of each incubation, bottles were filtered under low vacuum (5-10 in. Hg) over pre-combusted
 265 Whatman GF/F filters (450°C; 6h). Filters were stored at -20°C until further analysis on shore. NPP rates were
 266 quantified by measuring the incorporation of isotopically heavy carbon into phytoplankton biomass. Prior to
 267 measuring ^{13}C in the samples, filters were acid fumigated with concentrated HCl in a desiccator overnight to remove
 268 inorganic carbon. They were dried in an oven at 60°C for 24 h, individually wrapped in tin capsules and analyzed on
 269 a Carlo Erba NC2500 elemental analyzer interfaced with a Thermo Delta V+ isotope ratio mass spectrometer. The δ
 270 ^{13}C values were reported relative to the international standard Vienna PeeDee Belemnite (Coplen, 1995) and
 271 converted to atom percent values.

272 NPP rates were calculated from atom percent values with the equation from Hama et al. (1983)

$$NPP = \frac{POC \cdot (a_{is} - a_{ns})}{t \cdot (a_{ic} - a_{ns})} \quad (6)$$

274 where NPP is the net primary production rate ($\mu\text{g} \cdot \text{L}^{-1} \cdot \text{day}^{-1}$), POC is the particulate organic carbon; ($\mu\text{g} \cdot \text{L}^{-1}$), t is
 275 the incubation time (h), a_{is} is the atom % of ^{13}C in the incubated sample, a_{ns} is the atom % of ^{13}C in the natural
 276 sample (un-spiked sample described above) and a_{ic} is the atom % of ^{13}C in the total DIC pool. POC measurements
 277 were blank corrected with the mean value of triplicate combusted filter blanks. The DIC concentration was
 278 determined from salinity (S) according to the following equation from Parsons et al. (1984):

$$DIC = ((S * 0.067) - 0.05) * 0.96 \quad (7)$$

280 NPP rates were integrated to the depth of the mixed layer (Table S3) to align with NCP and GOP integrated rate
 281 calculations. In summer, NPP rates below 16 m (deepest mixed layer depth) were not used in this study.

282 No discrete measurements of net primary productivity (NPP) were conducted during the summer of 2018.
 283 However, we were able to estimate 2018 NPP rates as follows: For each summer, we computed phytoplankton
 284 biomass production (PP, $\text{mg C m}^{-3} \text{ d}^{-1}$) based on surface discrete Chl-a concentration and growth/grazing rates,
 285 following the methodology outlined by Landry et al. (2003). Chl-a concentrations were transformed into biomass
 286 using a constant C:Chl-a ratio of 50. In the summers from 2019 to 2022, where discrete NPP data were available, we
 287 averaged surface PP and surface NPP by region (inner-shelf, mid-shelf, and outer-shelf) and conducted a linear
 288 regression between these average PP and NPP rates ($p < 0.05$; $R^2 = 0.68$; $n = 15$). The linear regression coefficient
 289 obtained from this correlation was used to convert PP derived from growth/grazing rates in the summer of 2018 into
 290 NPP ($\text{mg C m}^{-3} \text{ d}^{-1}$). Subsequently, we integrated NPP over the mixed layer to obtain integrated NPP ($\text{mg C m}^{-2} \text{ d}^{-1}$)
 291 at each station where surface growth/grazing rates were available. While the C:Chl ratios in coastal systems exhibit
 292 high seasonal variability (Jakobsen and Markager, 2016), we used a constant C:Chl ratio when converting Chl-a into
 293 phytoplankton biomass. Since our comparison of derived PP was limited to the summer season, it is reasonable to
 294 assume that C:Chl ratios remained within a similar range. Additionally, the same C:Chl ratio was used when
 295 deriving the linear relationship and when applying it and thus the estimated NPP rates are insensitive to the choice of
 296 C:Chl ratio. It is important to note that C:Chl ratios were not utilized in the calculation of NPP rates for any other
 297 year.

298 2.4 Autotrophic and Heterotrophic Respiration

299 Assuming a photosynthetic quotient (O:C ratio) of 1.4, respiration rates were calculated from the productivity values
 300 (GOP, NPP, and NCP) and following the relationships below:

301
$$NPP = GOP - R_A \quad (8)$$

302
$$NCP = NPP - R_H \quad (9)$$

303 where R_A is autotrophic respiration and R_H is heterotrophic respiration.

304 2.5 Growth Rates and Grazing rates

305 Rates of phytoplankton growth and protistan grazing were quantified with a 2-point modification of the dilution
306 method (Landry et al., 2008; Chen, 2015; Morison et al., 2020) following methods in Marrec et al. (2021). Briefly,
307 surface samples were collected at 4 to 7 stations throughout the cruise. For each sample, whole seawater (WSW)
308 from the Niskin bottles was transferred into a 10-L polycarbonate carboy through a 200- μm mesh filter to remove
309 mesozooplankton predators. Diluent was prepared by gravity filtration through a 0.2 μm membrane filter capsule
310 (PALL®) from the Niskin to the carboys and mixed with WSW to obtain a 20% WSW dilution. A total of 6 bottles
311 per experiment were prepared: 2 bottles with nutrient amended 20% WSW, 2 bottles with nutrient-amended WSW,
312 and 2 bottles with unamended WSW to assess nutrient limitation. Incubations took place for 24 h in a clear, 1m³
313 deck-board incubator. Paired bottles were placed into mesh bags that simulated the effective light availability in the
314 surface mixed layer, which corresponded to 65% of sea surface irradiance. Phytoplankton growth and grazing
315 mortality rates were then estimated from changes in Chl-a over the 24 h incubation. For dilution experiments, Chl-a
316 concentrations were obtained from triplicate 150-mL subsamples filtered on GF/F filters, after a 12-h dark extraction
317 period at room temperature in 95% ethanol and measured on a calibrated Turner 10 AU fluorometer. The full
318 extraction method is detailed in Marrec et al. (2021).

319 2.6 Discrete Chlorophyll-a sample collection and processing

320 Samples for Chl-a analysis were collected into brown amber bottles from Niskins on the CTD Rosette system. A
321 known sample volume (250-500 mL) was filtered at low pressure (5-10 in. Hg) through either a GF/F filter or a 20
322 μm polycarbonate Sterlitech filter. Filters were transferred to either tissue capsules (GF/F) or cryogenic vials (20
323 μm) and then flash frozen in liquid nitrogen until extraction. Later, filters were extracted in 5 mL of 90% acetone for
324 24 hours in a dark refrigerator, then tubes were vortexed and centrifuged (only GF/F filters), and the solution was
325 measured on a calibrated Turner Designs Handheld Aquaflor fluorometer, acidified with 2 drops of 10%
326 hydrochloric acid and measured again. Chl-a concentrations for different size fractions were calculated by
327 difference. Note that in this study we consider large phytoplankton are as $> 20 \mu\text{m}$.

328 2.7 Satellite and radar data

329 To look at variability in SST and surface Chl-a, a proxy for phytoplankton biomass, throughout the summers over
330 multiple years, on a wider spatial and temporal scale than the at-sea chlorophyll data permitted, SST and surface
331 Chl-a concentrations from remote sensing sources were retrieved and analyzed. In particular, both snapshots and
332 monthly averages of MODIS (Moderate Resolution Imaging Spectroradiometer) SST and chlorophyll data with a
333 horizontal resolution of 1 km were used to examine the spatial coverage of the *Hemiaulus* bloom in summer 2019
334 (when it dominated phytoplankton biomass) and compare the surface temperature and chlorophyll in the NES region
335 in summers 2018-2022.

336 To examine possible origins of the bloom water, backward particle trajectory simulations were carried out
337 with the OceanParcels Python package <https://oceanparcels.org/index.html> (Lange and Van Sebille, 2017). High
338 frequency (HF) radar-measured sea surface velocity data in the NES region in Jul-Aug 2019 with 6-km spatial
339 resolution and hourly temporal resolution were used as the background flow. Particles were released at mid-shelf
340 sites along the NES-LTER transect on Aug 21, 2019 and advected backward for 30 days until Jul 22, 2019.

341 2.8 Imaging FlowCytobot

342 Composition of the phytoplankton community was assessed with Imaging FlowCytobots (IFCB; McLane Research
343 Laboratories, Inc.). IFCB uses a combination of video and flow cytometry technology to capture images of plankton
344 and other particles in the size range ~ 5 -150 μm (Olson and Sosik, 2007). During the cruises reported here, IFCB
345 instruments were configured to record images of particles with laser-based chlorophyll fluorescence or light
346 scattering signals above trigger thresholds and samples were pre-screened with 150 μm Nitex. IFCB instruments
347 were operated two ways. First, on all cruises, an IFCB was configured to sample 5 mL automatically from the ship's

348 underway system every 25 minutes. Second, at stations occupied on the NES-LTER and SPIROPA cruises, IFCB
349 instruments were used to analyze depth profiles from discrete samples collected with Niskin bottles. Typically, three
350 5-mL subsamples were measured for each depth. The fraction of each 5-mL sample imaged by IFCB decreases with
351 increasing trigger rate but is recorded precisely during sample acquisition enabling calculation of concentrations.
352 IFCB image data were automatically analyzed following approaches developed for the IFCB time series at the
353 Martha's Vineyard Coastal Observatory (MVCO) (Brownlee et al., 2016). In particular, cell biovolume was
354 estimated from IFCB images (Moberg and Sosik, 2012) and converted to cell carbon following the relationships
355 described by Menden-Deuer and Lessard (2000). IFCB images were classified with a convolutional neural network
356 (CNN) (Catlett et al., 2023) trained to separate 155 categories of plankton and other particles observed at MVCO
357 and across the NES region. We used the Inception v3 (Szegedy et al., 2016) CNN architecture as implemented in
358 PyTorch, pre-trained with ImageNet (Russakovsky et al., 2015) and fine-tuned with an NES IFCB training set
359 (97026 images, 155 classes, 80-20 split for training and validation). In addition, an independent test set of manually
360 annotated images in 51 IFCB samples from EcoMon cruises was used to evaluate *Hemiaulus* quantification as a
361 function of classifier score threshold. From this independent analysis, classifier predictions with scores above 0.9
362 performed very well for *Hemiaulus* (class-specific F1-score = 0.936; CNN-count vs. manual-count: $r^2 = 0.999$, slope
363 = 0.915; intercept = 0.005).

364 2.9 Nutrients

365 Dissolved inorganic nutrient concentrations (ammonium, phosphate, silicate, and nitrate + nitrite) were obtained
366 from CTD bottle samples with duplicates. Seawater was passed through an EMD Millipore sterile Sterivex 0.22 μm
367 filter with filtrate collected into acid-washed 20-ml scintillation vials (after triplicate rinses), which were then stored
368 at $-20\text{ }^\circ\text{C}$ until analysis. Samples were processed at Woods Hole Oceanographic Institution's Nutrient Analytical
369 Facility with a four-channel segmented flow SEAL AA3 HR Autoanalyzer. Detection levels are as follows: 0.01
370 $\mu\text{mol L}^{-1}$ for silicate, 0.03 $\mu\text{mol L}^{-1}$ for phosphate, 0.04 $\mu\text{mol L}^{-1}$ for nitrate + nitrite, and 0.03 $\mu\text{mol L}^{-1}$ for
371 ammonium.

372 3 Results

373 3.1 *Hemiaulus* distribution and Chlorophyll

374 During the NES-LTER summer 2019 cruise, through automated image classification and analysis and through visual
375 microscopic confirmation, a bloom of the diatom genus *Hemiaulus* was observed in the surface waters of the mid-
376 shelf region (Fig. 2a). These images also showed N_2 fixing symbionts, namely *Richelia*, inside or next to the

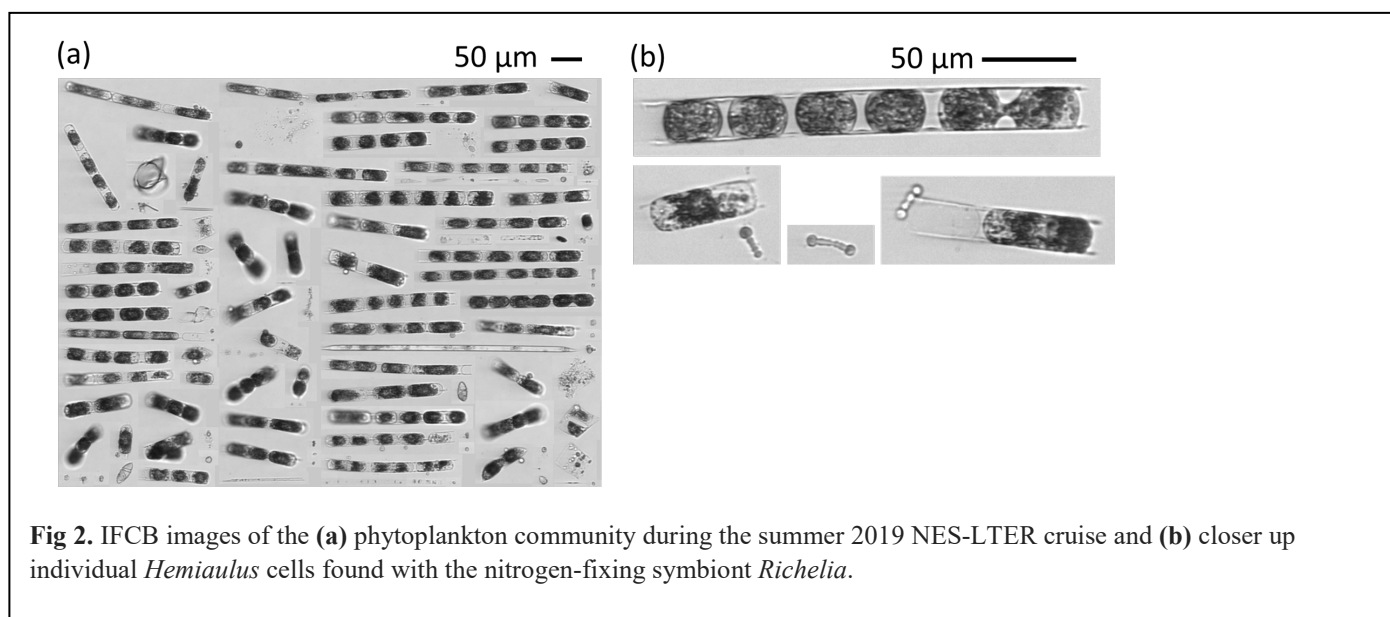


Fig 2. IFCB images of the (a) phytoplankton community during the summer 2019 NES-LTER cruise and (b) closer up individual *Hemiaulus* cells found with the nitrogen-fixing symbiont *Richelia*.

377 *Hemiaulus* cells (Fig. 2b). Additionally,
 378 *Hemiaulus* carbon was highest in the mid-
 379 shelf waters between latitudes of 40.1° N
 380 and 41.1° N, a span of 111 km (Fig. 3a),
 381 with concentrations ranging from 6.8 to
 382 68.3 $\mu\text{g L}^{-1}$. This bloom was only observed
 383 in the surface waters of the mid-shelf
 384 region, as can be seen by discrete IFCB
 385 measurements from Niskin samples (Fig.
 386 3b). *Hemiaulus* carbon concentrations
 387 observed in other years on NES-LTER
 388 transect cruises never reached values above
 389 0.30 $\mu\text{g L}^{-1}$, so approximately two orders of
 390 magnitude smaller than was observed on
 391 the 2019 cruise. Furthermore, IFCB-based
 392 observations made on a broader scale from
 393 the mid-Atlantic bight to the Gulf of Maine
 394 in the period from 2013 to 2023, show that
 395 only in August 2019 is *Hemiaulus* present
 396 in large quantities (Fig. S1), confirming the
 397 extraordinary nature of the 2019 bloom.

398 The presence of the diatom bloom
 399 was consistent with the size-fractionated
 400 Chl-a data. Surface Chl-a concentrations in
 401 the mid-shelf region in summer are
 402 typically low ($< 0.50 \mu\text{g L}^{-1}$, Fig. 4a) and
 403 progressively decrease with decreasing
 404 latitude. During the NES-LTER summer
 405 2019, however, Chl-a concentrations were
 406 as high as $3.50 \mu\text{g L}^{-1}$ in the surface waters
 407 of the mid-shelf (mean Chl-a of $1.97 \mu\text{g L}^{-1}$,
 408 Table 2) with up to 80% of the Chl-a
 409 associated with the $> 20 \mu\text{m}$ fraction (Fig.
 410 4c). This is in contrast to other summers
 411 when most of the Chl-a was associated
 412 with the $< 20 \mu\text{m}$ fraction (Fig. 4b, d-f).
 413 Concentrations of Chl-a in the $> 20 \mu\text{m}$
 414 size fraction and concentrations of
 415 *Hemiaulus* carbon in the NES-LTER
 416 summer 2019 cruise were larger at co-
 417 located sampling locations in the beginning
 418 of the cruise than at the end, suggesting that
 419 the bloom may have peaked before the cruise
 420 started and thus was in decline during the
 421 cruise period.

422 Monthly mean surface Chl-a concentrations
 423 from remote sensing were used to investigate
 424 if the observed differences in Chl-a and
 425 productivity between the summers were
 426 related to differences in the timing of the
 427 cruise as opposed to differences in
 428 community composition (Fig. S3). In many
 429 of the summers (2018, 2021, and 2022),
 430 Chl-a in July was actually higher than in
 431 August, suggesting that the timing of the
 432 2019 cruise (end of August instead of end
 433 of July) was not a factor in explaining the
 434 anomalously high productivity observed in
 435 August, 2019. If anything, the change in
 436 timing of the 2019 NES-LTER cruise would
 437 lead us to expect the Chl-a to be lower in
 438 August than in July and thus the high Chl-a
 439 observed in August, 2019 is even more
 440 startling. Satellite data cannot be used to
 441 confirm the presence or absence of
 442 *Hemiaulus*. However, IFCB data from NES
 443 broadscale NOAA EcoMon surveys from
 444 summer 2013 to 2023, many of which
 445 occurred in August, always showed minimal
 446 presence of *Hemiaulus*, suggesting the
 447 observed bloom in August 2019 was indeed
 448 extraordinary and not simply related to the
 449 timing of the 2019 LTER cruise (Fig. S1).

430
431

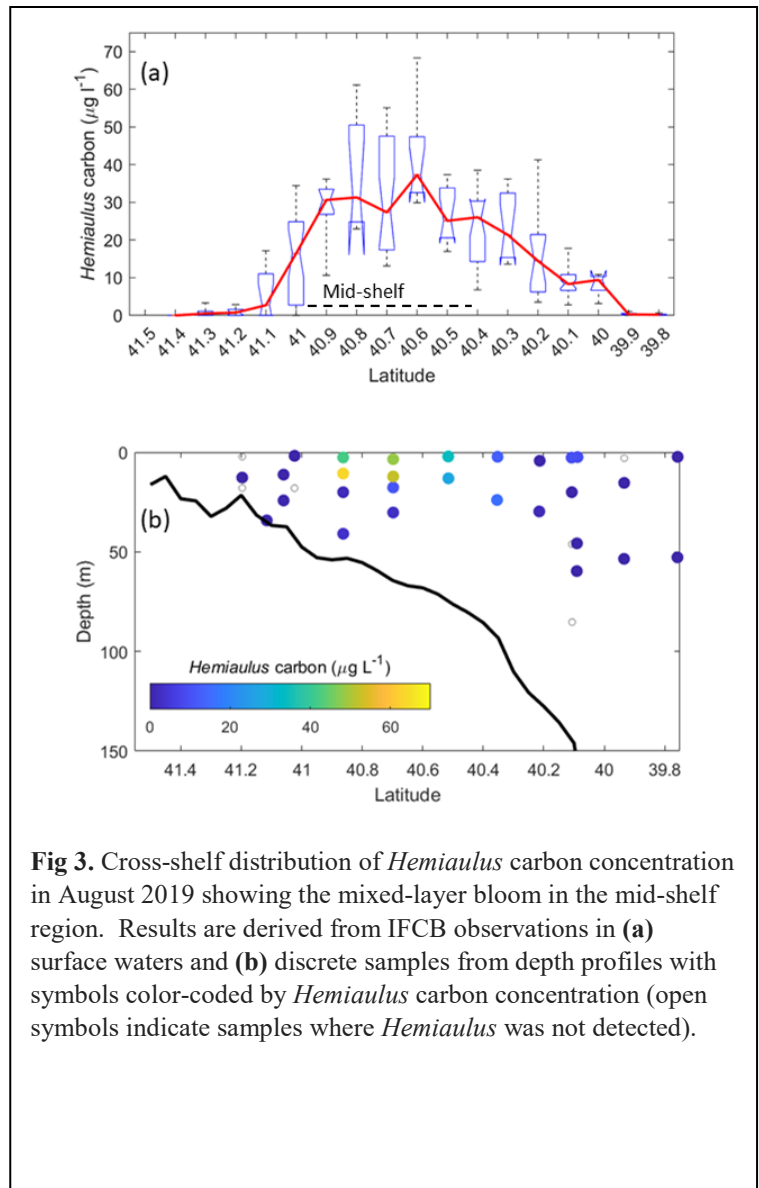


Fig 3. Cross-shelf distribution of *Hemiaulus* carbon concentration in August 2019 showing the mixed-layer bloom in the mid-shelf region. Results are derived from IFCB observations in (a) surface waters and (b) discrete samples from depth profiles with symbols color-coded by *Hemiaulus* carbon concentration (open symbols indicate samples where *Hemiaulus* was not detected).

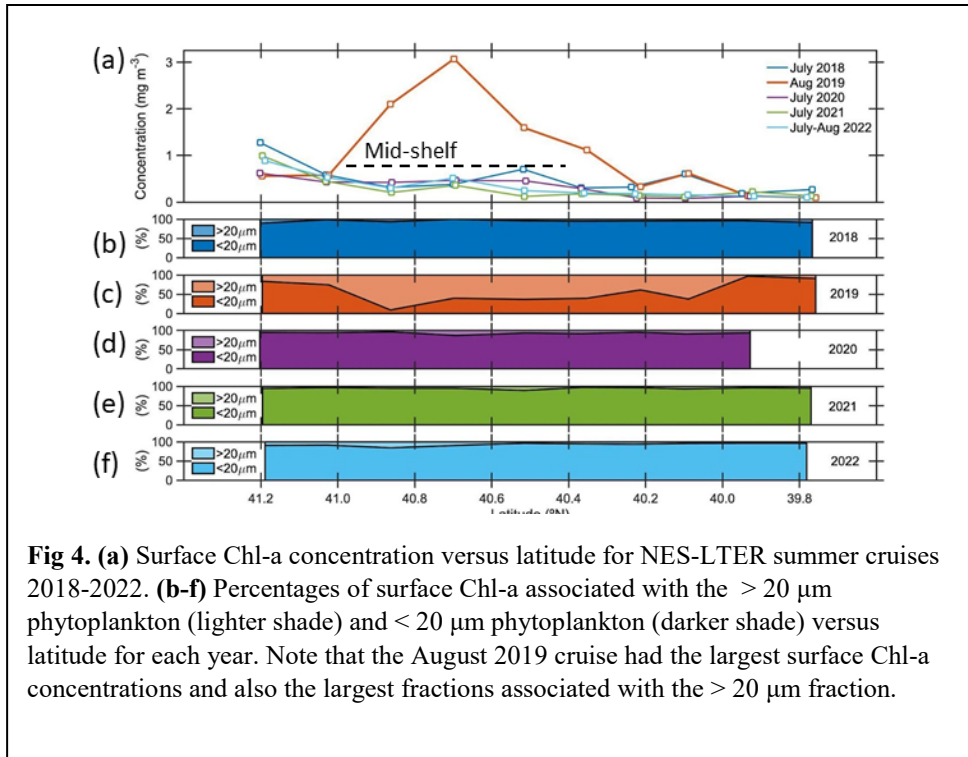
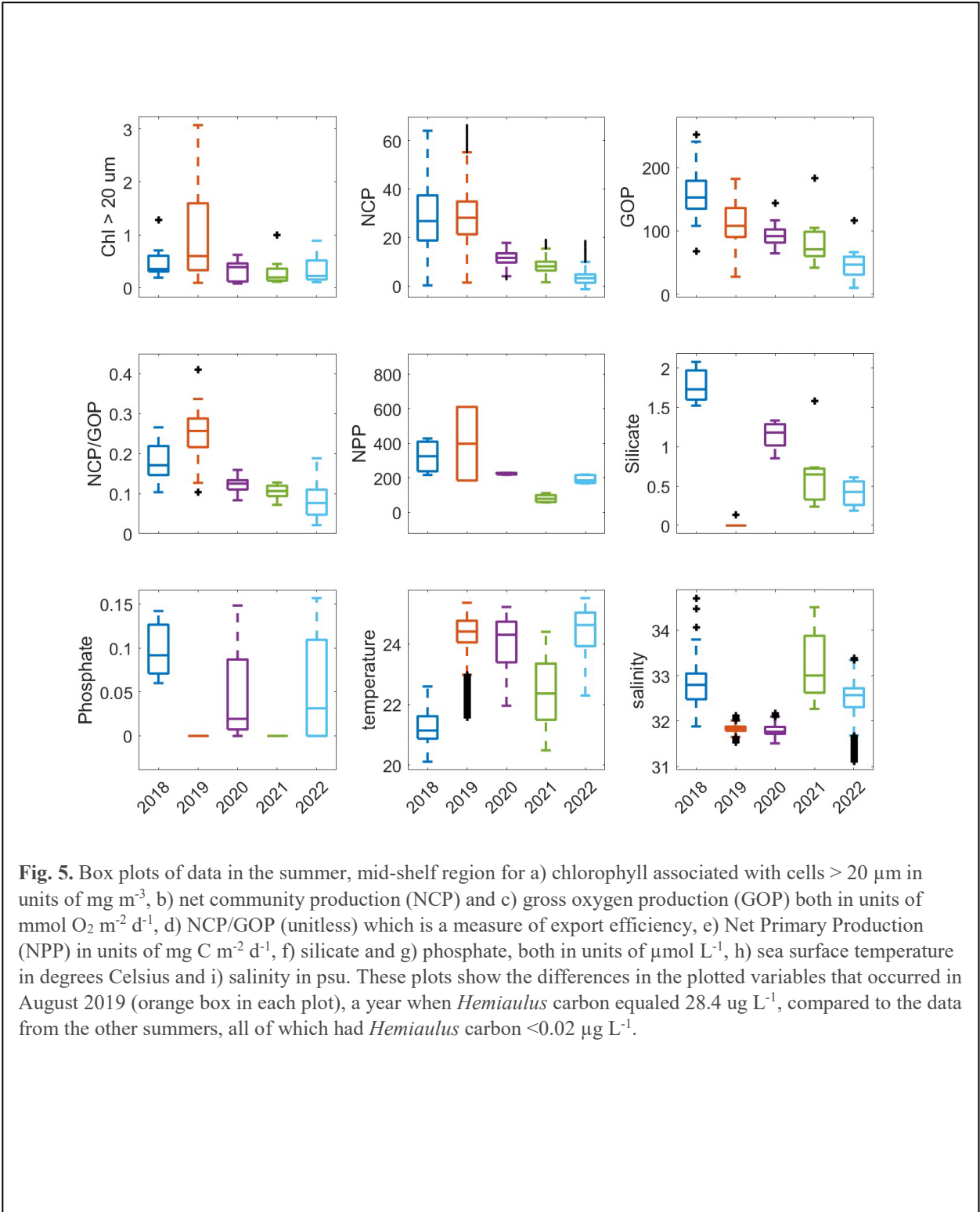


Fig 4. (a) Surface Chl-a concentration versus latitude for NES-LTER summer cruises 2018-2022. **(b-f)** Percentages of surface Chl-a associated with the $> 20 \mu\text{m}$ phytoplankton (lighter shade) and $< 20 \mu\text{m}$ phytoplankton (darker shade) versus latitude for each year. Note that the August 2019 cruise had the largest surface Chl-a concentrations and also the largest fractions associated with the $> 20 \mu\text{m}$ fraction.

432 3.2 Physical properties

433 During the NES-LTER summer 2019 cruise, SST in the mid-shelf region was only slightly higher than during most
 434 of the other summer cruises (Table 2, Fig. 5). In contrast, SST in summer 2019 on the outer-shelf region in
 435 particular was substantially higher than on any other summer cruise (Fig. 6a). Notably, the 2019 cruise occurred
 436 later in the summer season (August) than the NES-LTER cruises in other years (July). Along the NES-LTER
 437 transect specifically, SST in July 2019 was lower than in August 2019 and was similar to other years. In general,
 438 monthly-averaged satellite SST data in the broader NES region usually showed lower SST values in July compared
 439 to August (2018, 2020-2022) (Fig. S3). Interestingly, however, in summer 2019, the monthly averaged satellite data
 440 actually showed higher SST in July, because of impingement of a Gulf Stream warm-core ring on the shelf edge
 441 (Zhang et al., 2023) and the subsequent onshore intrusion of the ring water in July 2019. The fact that monthly
 442 averaged satellite SST was higher in July than August but the local NES-LTER transect data had higher temperature
 443 in August than July suggests that the high SST observed during late August 2019 reflected an ephemeral event and
 444 not a mean condition during that month. Despite the occurrence of the NES-LTER summer 2019 cruise during a
 445 specific week of August and conditions that suggest an ephemeral event, for simplicity, we will refer to it as August
 446 2019 in this paper. During the NES-LTER August 2019 cruise, surface salinity was lower than on 2018, 2021, and
 447 2022 summer cruises, but similar to surface salinity during the July 2020 cruise (Fig. 5, Fig. 6b) and to salinities
 448 observed in July 2019 along the NES-LTER transect
 449



451 **Table 2.** Averages, standard errors, and number of measurements (n) of surface mixed layer characteristics (productivity values integrated through the surface
 452 mixed layer; physical conditions, nutrients, and Chl-a concentrations from the surface) in the mid-shelf region (70.883° W, 40.437°N - 40.980°N, water depth
 453 50 to 100 m) measured during NES-LTER summer cruises for each year. The last columns show the mean data for winter NES-LTER cruises 2018-2022 in the
 454 same mid-shelf region. The NPP average in 2018 (*) was calculated based on the phytoplankton growth rate since direct NPP measurements were not available
 455 for this year – see text for details.

456

	2018			2019			2020			2021			2022			All winters		
	mean	std	n	mean	std	n	mean	std	n	mean	std	n	mean	std	n	mean	std	N
NCP (mmol O ₂ m ⁻² d ⁻¹)	28.8	0.2	4816	28.8	0.2	5446	11.3	0.1	2895	8.4	0.05	6120	3.8	0.1	5763	5.1	0.1	29258
GOP (mmol O ₂ m ⁻² d ⁻¹)	160	10	19	110	9	22	100	7	17	104	26	12	40	5	28	101	20	89
NCP//GOP	0.18	0.01	19	0.24	0.09	22	0.13	0.01	17	0.09	0.01	12	0.07	0.01	28	0.11	0.04	89
NPP (mg C m ⁻² d ⁻¹)	* 324	20	*4	398	213	2	225	4	3	81	10	6	191	10	6	464	63	11
Phytoplankton growth rate (d ⁻¹)	1.12	0.11	4	0.2	0.17	2	0.8	0.10	2	0.83	0.64	2	0.31	0.1	2	0.3	0.04	18
Micro-zoop. grazing (d ⁻¹)	0.19	0.03	4	0.17	0.04	2	0.22	0.09	2	0.51	0.25	2	0.11	0.05	2	0.24	0.05	18
Temperature (°C)	21.44	0.01	4816	24.29	0.01	5446	23.88	0.02	2895	22.61	0.02	6120	24.46	0.01	5763	6.131	0.007	29258
Salinity (psu)	32.71	0.01	4816	31.83	0.001	5446	31.8	0.002	2895	33.17	0.01	6120	32.53	0.01	5763	32.79	0.002	29258
<i>Hemiaulus</i> Carbon (µg L ⁻¹)	0.002	0.002	93	28.4	1.3	102	0	0.00	65	0.001	0.001	113	0.003	0.003	104	0.018	0.006	562
Chl-a (mg m ⁻³)	0.43	0.10	8	1.97	0.59	8	0.4	0.06	8	0.22	0.07	8	0.32	0.10	8	2.17	0.16	40?
%Chl-a >20 µm	0.02	0.006	8	1.37	0.43	8	0.03	0.01	8	0.01	0.004	8	0.03	0.02	8	1.56	0.14	38
Silicate (µmol L ⁻¹)	1.9	0.3	8?	0.27	0.5	8?	1.4	0.5	8?	0.75	0.4	8?	0.42	0.18	8?	1.7	0.5	40
Phosphate (µmol L ⁻¹)	0.11	0.01	8?	0.025	0.02	8?	0.085	0.10	8?	0	0.00	8?	0.06	0.06	8?	0.5	0.30	40

457

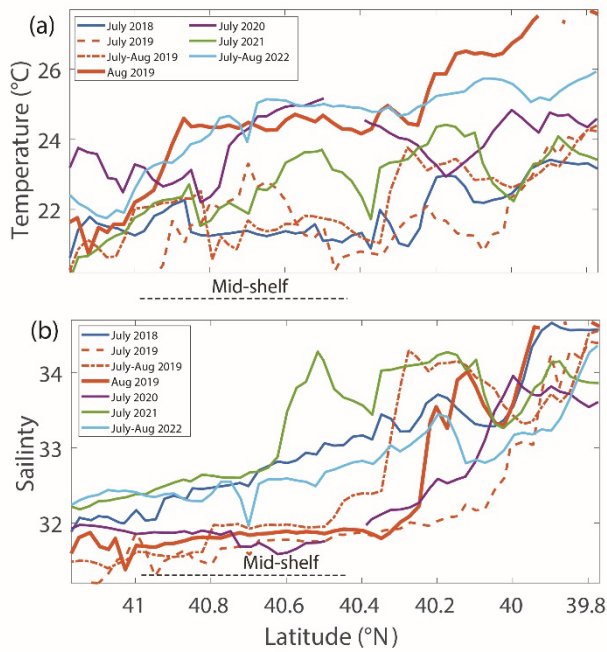


Fig 6. (a) Temperature and **(b)** salinity 5 m below the surface versus latitude for NES-LTER summer cruises (2018-2022) and the SPIROPA and OTZ summer 2019 cruises. For clarity, the values are averaged in 0.025 degree latitude bands when there were multiple occupations of the same region. The mid-shelf region is denoted by a dashed line.

481

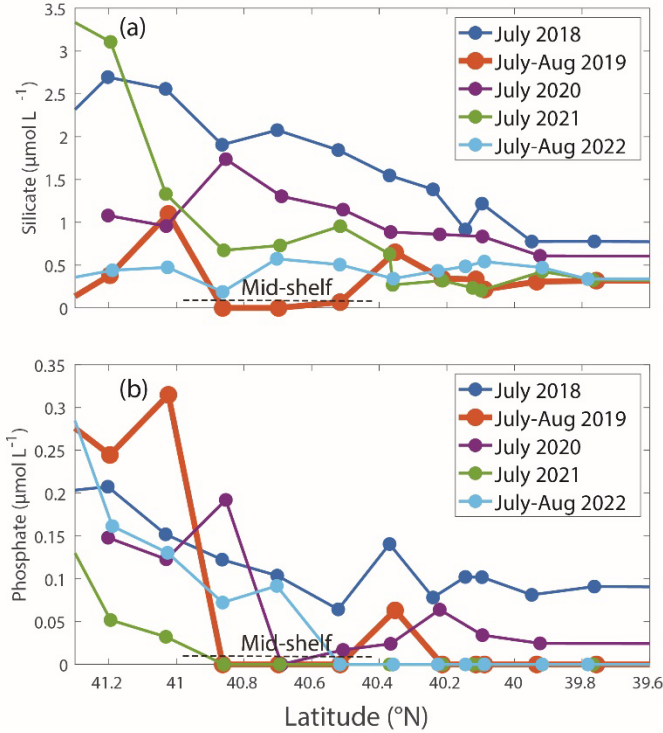


Fig 7. (a) Silicate and **(b)** phosphate concentrations (in $\mu\text{mol L}^{-1}$) in the upper 12 m of the water column for NES-LTER summer cruises (2018-2022). The mid-shelf region is denoted by a dashed line.

494

495 3.3 Nutrients

496 Nutrient concentrations differed between the August 2019 cruise and other summer cruises. Specifically, phosphate
 497 and silicate concentrations in surface waters were lower in August 2019 compared to most other summers (Table 2,
 498 Fig. 5, Fig. 7). In other summers, silicate decreased with distance from shore, but in 2019, silicate was depleted
 499 between 41°N and 40.4°N (Fig. 7a) coincident with the location of the *Hemiaulus* bloom. Additionally, higher
 500 levels of silicate were found around depths of 50 m to 140 m in August 2019 than during other summer NES-LTER
 501 cruises (Fig. S4), which may be associated with diatoms that had sunk and were starting to be remineralized,
 502 releasing silicate back into the water column. Surface water phosphate concentrations in August 2019 were depleted
 503 south of 41° N (Fig. 7b). However, low concentrations of phosphate were also found in summer of 2021. Lastly,
 504 while nitrate plus nitrite were measured on the same samples as phosphate and silicate, nitrate + nitrite
 505 concentrations were close to the detection level in the surface samples for all summer cruises except a few stations
 506 in 2018 and thus are not shown here. Ammonium levels are not discussed because the samples were frozen at sea
 507 and thus may not be reliable; additionally, ammonium levels showed no clear relationship over the transect cruises.

509 3.4 Productivity and grazing rates

510 In August 2018 NCP was
 511 elevated in the mid-shelf waters,
 512 coincident with the location of the
 513 *Hemiaulus* bloom (Fig. 1). NCP
 514 peaked in the first half of the
 515 cruise and decreased during the
 516 second half, supporting the earlier
 517 supposition that the *Hemiaulus*
 518 bloom was likely in decline (Fig.
 519 S2). Additionally, the area of
 520 maximum NCP moved shoreward
 521 in the second half of the cruise.
 522 The high NCP was primarily
 523 constrained to the main longitude
 524 sampling line and usually did not
 525 extend, at least at those points in
 526 time, spatially off the main
 527 transect.

528 During August 2019,
 529 waters with high carbon
 530 concentrations of *Hemiaulus*
 531 showed higher rates of NCP (Fig.
 532 8a), NCP/GOP (Fig. 8b), GOP
 533 (Fig. 8c), and NPP (Fig. 8d)
 534 compared to these rates at mid-
 535 shelf waters in most other years
 536 (Fig. 5). More specifically, the
 537 mid-shelf waters where
 538 *Hemiaulus* was present in Aug
 539 2019 displayed NCP values
 540 approximately 2.5 to 9 times
 541 larger than in the same mid-shelf
 542 latitudes in summers of 2020-22
 543 (Table 2). Furthermore, we
 544 observed a correlation between NCP and *Hemiaulus* carbon between Aug 21 and Aug 23 (Fig. 9; $R^2 = 0.54$, $p <$

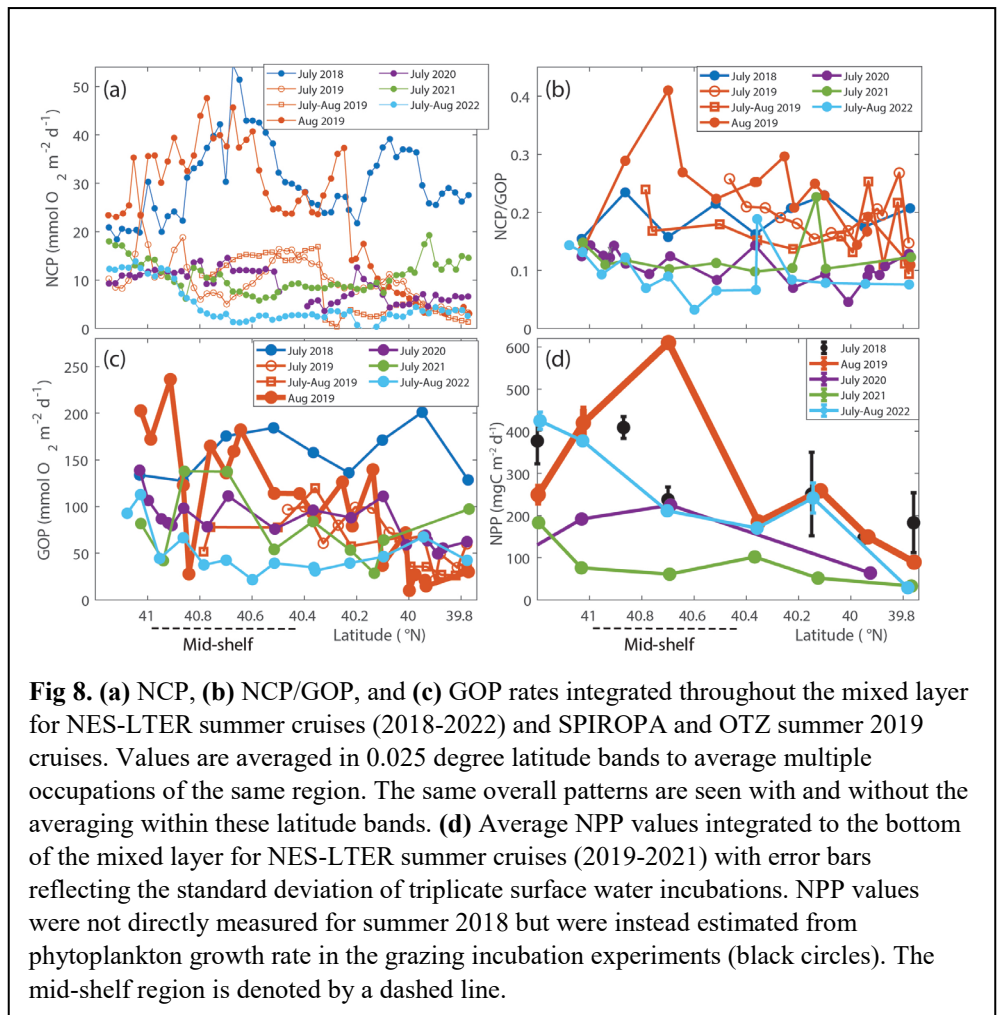


Fig 8. (a) NCP, (b) NCP/GOP, and (c) GOP rates integrated throughout the mixed layer for NES-LTER summer cruises (2018-2022) and SPIROPA and OTZ summer 2019 cruises. Values are averaged in 0.025 degree latitude bands to average multiple occupations of the same region. The same overall patterns are seen with and without the averaging within these latitude bands. (d) Average NPP values integrated to the bottom of the mixed layer for NES-LTER summer cruises (2019-2021) with error bars reflecting the standard deviation of triplicate surface water incubations. NPP values were not directly measured for summer 2018 but were instead estimated from phytoplankton growth rate in the grazing incubation experiments (black circles). The mid-shelf region is denoted by a dashed line.

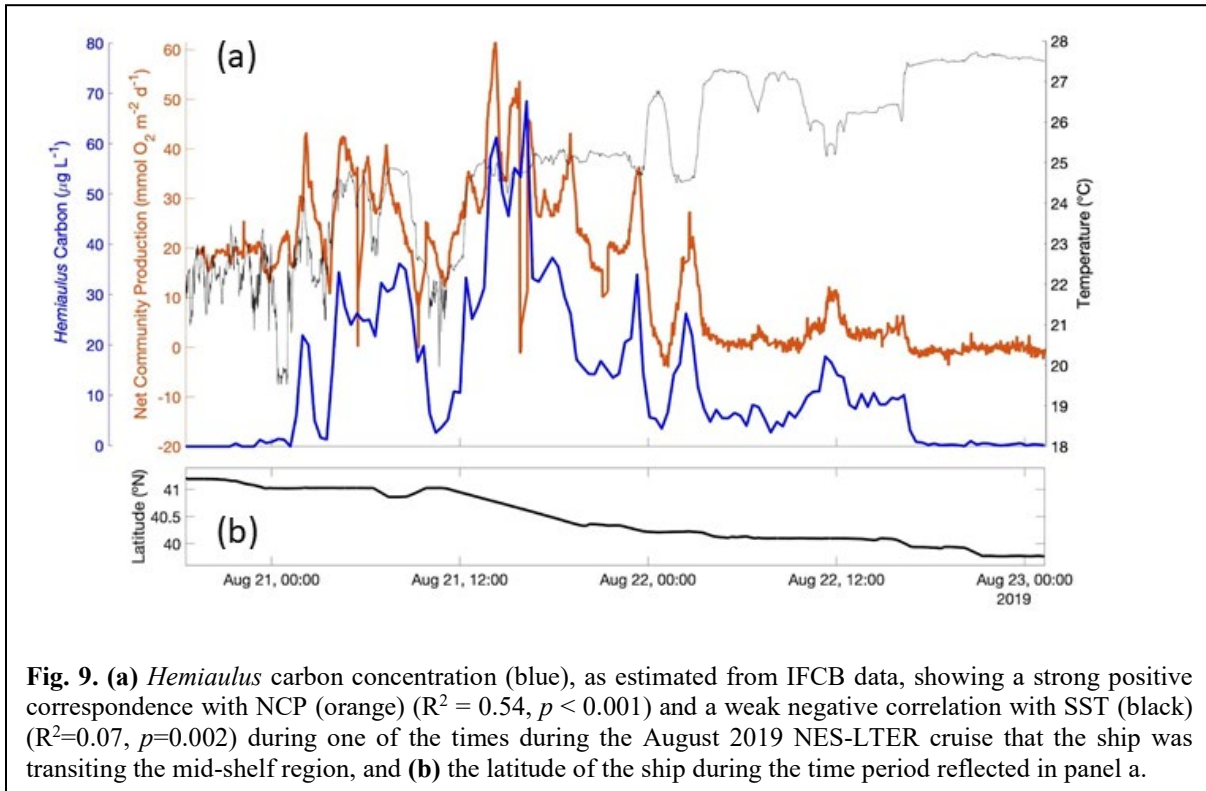


Fig. 9. (a) *Hemiaulus* carbon concentration (blue), as estimated from IFCB data, showing a strong positive correspondence with NCP (orange) ($R^2 = 0.54$, $p < 0.001$) and a weak negative correlation with SST (black) ($R^2=0.07$, $p=0.002$) during one of the times during the August 2019 NES-LTER cruise that the ship was transiting the mid-shelf region, and **(b)** the latitude of the ship during the time period reflected in panel a.

545 0.001). The patchiness of the diatom bloom corresponded to the patchiness in NCP. Additionally, cooler shelf water
 546 was associated with higher abundances of *Hemiaulus* than the warmer slope water (Fig. 9), suggesting a water mass
 547 dependence on the location of the *Hemiaulus* bloom. Thus, the patchiness in the bloom and NCP is likely a result of
 548 the ship crossing different water masses.

549 GOP rates were only slightly higher in summer 2019 than in other summers (Fig. 5 and 8c). In particular,
 550 GOP rates were higher by a factor of 1.1 in waters with the *Hemiaulus* bloom in 2019 than during the summers of
 551 2020-21; GOP rates were much higher in August 2019 than in summer of 2022 by a factor of 2.75. Notably, NCP,
 552 GOP, and NCP/GOP rates in summer 2018 were comparable to these rates in August 2019 (discussed below in
 553 section 4.1).

554 Additionally, within the region that corresponds directly with the location of the *Hemiaulus* bloom, NPP
 555 rates in 2019 were ~1.5 - 2.5 times higher than NPP rates during other summer cruises. (Fig. 8d; Table 2). More
 556 specifically, NPP at 40.7 $^{\circ}\text{N}$ was approximately double the NPP measured in 2020 and more than double the rate
 557 measured in 2021. Furthermore, at 40.4 $^{\circ}\text{N}$, NPP in 2019 was about 40% higher than in 2021 (no data for this station
 558 in 2020) (Fig. 8d).

559 A larger difference between NCP in the various summers than between GOP in the summers suggests that
 560 the increase in NCP in August 2019 was due to both increased photosynthesis and decreased community respiration.
 561 In a rough approximation, we calculated autotrophic respiration and heterotrophic respiration to show that
 562 autotrophic respiration was lower than average in August 2019 ($R_A = 308 \text{ mg C m}^{-2} \text{ d}^{-1}$ in August 2019 versus 496
 563 $\text{mgC m}^{-2} \text{ d}^{-1}$ average for the other summers). This approach also showed that heterotrophic respiration was higher
 564 than average in August 2019 ($431 \text{ mgC m}^{-2} \text{ d}^{-1}$ in August 2019 versus 247 $\text{mg C m}^{-2} \text{ d}^{-1}$ average for the other
 565 summers). Note this estimation is highly uncertain due to the different time and spatial scales associated with the gas
 566 tracers used to quantify NCP and GOP and the incubation techniques used for NPP.

567 Since the summer 2019 NES-LTER cruise occurred in the middle of August rather than in mid to late July
 568 as was typical for most other summers, the physical conditions were inherently different in 2019. We compared
 569 NCP and GOP data (NPP not available) from two earlier cruises in summer 2019 (cruise details in Table 1) whose
 570 cruise track in the mid-shelf region overlapped with those of the LTER cruise, i.e. followed the same longitude
 571 70.883 $^{\circ}\text{W}$. These cruises occurred before the *Hemiaulus* bloom and while their IFCB records showed a detection of
 572 *Hemiaulus*, the abundance of this diatom was very low ($< 1 \mu\text{gC L}^{-1}$). These two July 2019 cruises had much lower
 573 NCP rates compared to August 2019, and specifically had rates similar to those observed in summer 2020-22 NES-

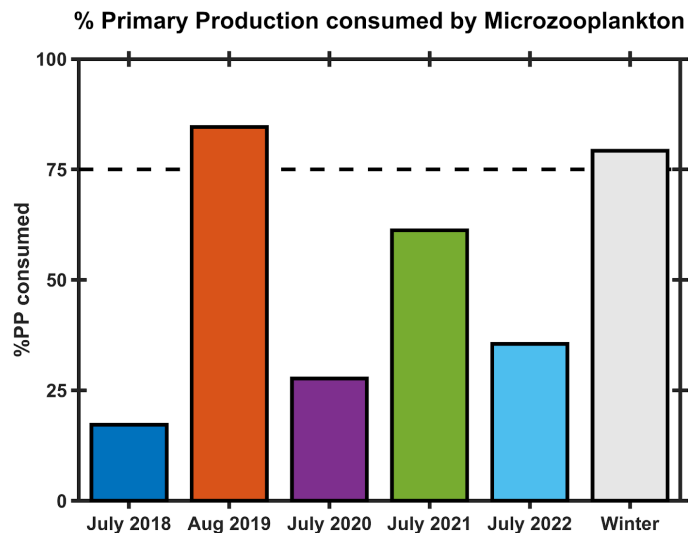


Fig 10. Percentage of primary production (%PP) consumed by microzooplankton in surface waters in the mid-shelf region during NES-LTER cruises for each summer and the overall average from NES-LTER winter cruises 2018-2022. %PP consumed by microzooplankton is calculated as the ratio of microzooplankton grazing rate (d^{-1}) to phytoplankton growth rate (d^{-1}).

574 LTER transect cruises (Fig. 8a & b). Together, these data suggest that higher production rates in 2019 were uniquely
 575 tied to the presence of *Hemiaulus* rather than representing deviations in timing or environmental conditions.

576 The ratio of protistan grazing to phytoplankton growth rates provides an estimate of the percent of primary
 577 production (%PP) consumed by microzooplankton (Fig. 10). In contrast to typical summer conditions ($> 0.6 d^{-1}$,
 578 Table 2), during August 2019, phytoplankton growth rates during the *Hemiaulus* bloom were low ($< 0.2 d^{-1}$, Table
 579 2) compared to other summers, with most of the primary production consumed by microzooplankton (%PP = 84%,
 580 Table 2). Notably, these low phytoplankton growth rates are in the same range as other diatoms with *Richelia*
 581 symbionts, namely $0.3 d^{-1}$ for *Rhizosolenia-Richelia* cultured at a similar temperature (Villareal, 1990). Thus in
 582 August 2019, phytoplankton growth and microzooplankton grazing were well coupled (though only in the part of the
 583 transect where *Hemiaulus* bloomed), like typical winter conditions, when the phytoplankton community structure is
 584 dominated by large cells, instead of the decoupling typically observed in most summer conditions dominated by
 585 picoplankton (Marrec et al., 2021). We note that coupling between phytoplankton growth and microzooplankton
 586 grazing was occasionally observed during other summer cruises, but mostly in inner-shelf waters (except one mid-
 587 shelf station in July 2021). Overall, most of the primary production during the *Hemiaulus* bloom was grazed by
 588 microzooplankton indicating high trophic transfer efficiency from phytoplankton to microzooplankton.

589 4 Discussion

590 4.1 Change in community composition altering biological rates

591 A bloom of *Hemiaulus* has not been observed on any previous NES-LTER cruise and to our knowledge,
 592 has not been reported in the broader NES region before. Additionally, only in August 2019, compared to summers
 593 2018 and 2020-22, most of the Chl-a was associated with the $> 20 \mu m$ size fraction. Thus, the presence of the diatom
 594 bloom found in August 2019 was a major change in phytoplankton composition observed in this region of the NES
 595 that likely led to the observed large changes in productivity rates and coupling between phytoplankton growth and
 596 grazing.

597 It is likely that the nitrogen-fixing symbionts in *Hemiaulus* allowed the diatom to thrive in the stratified,
 598 low nutrient surface waters of the summer shelf. This is supported by phosphate draw-down to levels below
 599 detection in August 2019; the nitrogen-fixing symbionts in the *Hemiaulus* likely made phosphate a limiting factor

600 for growth (Tang et al., 2020) in August 2019 whereas nitrate limitation is typical for NES summer conditions.
601 While the summer of 2021 also had very low phosphate, summer 2021 was different in that it also had low
602 productivity rates and more typical levels of silicate, suggesting the low phosphate occurred for fundamentally
603 different reasons in 2019 and 2021.

604 Silicate is especially important for diatoms because it is required for formation of their cell frustules.
605 Moreover, previous studies show that the availability of dissolved silica seems to be an important control for many
606 diatom-diazotroph blooms by affecting the growth rate and size of the diatom's frustules (Kemp and Villareal, 2013;
607 Spitzer, 2015). The observed depletion of silicate and phosphate in surface waters during the August 2019 cruise
608 suggests that, at the time of the cruise, the *Hemiaulus* bloom may have been in decline. The low phytoplankton
609 growth rates of 0.2 day^{-1} support the idea that the bloom had peaked, particularly given the fact that with sufficient
610 phosphate, silicate and light, the *Hemiaulus* DDA can achieve growth rates of $0.7\text{-}0.9 \text{ d}^{-1}$ in laboratory cultures (Pyle
611 et al., 2020). Low growth rates also could be attributed to the inverse relationship between phytoplankton cell size
612 and growth rate. The *Hemiaulus* population could have been limited by phosphate, silicate, or both. The higher
613 levels of silicate observed at depth in August 2019 are likely due to *Hemiaulus* sinking out of the euphotic zone and
614 frustule remineralization at depth, which would release the silicate—and other nutrients—back into the water (Twining
615 et al., 2014).

616 The strong coherence between the high spatial resolution data on *Hemiaulus* carbon concentrations and
617 NCP (Fig. 9), as well as the other data presented here and a clear potential mechanism, strongly support the idea that
618 the high productivity rates observed in August 2019 are directly due to the presence of *Hemiaulus*. In particular, the
619 high NCP rates observed during the August 2019 NES-LTER cruise and their overlap with the location of the
620 diatom bloom, suggest a high export ecosystem developed due to *Hemiaulus*' influence on productivity and
621 biological rates. Here, we define export as a flux away from the local biological production compartment, which can
622 include losses of carbon (or oxygen) to depth or transfer to higher trophic levels. While the *Hemiaulus* bloom
623 slightly increased total photosynthesis, as seen from the GOP rates, the bloom presence affected NCP, and thus by
624 extension, export production to a higher degree, potentially due to the large size of *Hemiaulus* cells and chains. The
625 NCP/GOP ratio in August 2019 was double the ratio observed in the summers 2020-22 (Table 2, Fig. 5). Other
626 studies have shown links between variations in NCP/GOP and changes in planktonic community composition
627 (Palevsky et al., 2016). Bigger phytoplankton cells sink faster than small ones, making them less likely to be grazed
628 before sinking out of the euphotic zone, allowing for a higher export efficiency. Additionally, a higher trophic
629 transfer efficiency (see next paragraph) would also lead to a larger NCP/GOP ratio. Hence, the NES-LTER summer
630 2019 cruise appears to have represented a high carbon export efficiency system.

631 Not only did NCP and GOP rates change because of the *Hemiaulus* bloom, but so did NPP, phytoplankton
632 growth rates, chl-a concentrations, and the trophic transfer efficiency within the planktonic food web. The presence
633 of *Hemiaulus* in the mid-shelf region likely led to the observed higher NPP rates during August 2019 compared to
634 all other observed summers in the mid-shelf region of the NES (Fig. 5 and 8). High NPP rates associated with
635 diatom blooms have been observed in other systems such as on the Eastern Bering Shelf (Lomas et al., 2012) and in
636 the Gulf of California (Puigcorbe et al., 2015), including during blooms of, diatom-diazotroph associations such as
637 *Hemiaulus-Richelia* (Gaysina et al., 2019). For example, Tang et al. (2020) reported a high contribution of nitrogen
638 fixation to NPP off the coast of New Jersey during their 2015-2016 survey in the Western North Atlantic. Even
639 though high NPP was associated with the location of the *Hemiaulus* bloom in our study, phytoplankton growth rates
640 were low ($< 0.2 \text{ d}^{-1}$). This decoupling between NPP and growth was likely due to the order of magnitude higher chl-
641 a concentrations observed during August 2019 ($1.37 \mu\text{g L}^{-1}$) compared to other summers ($0.01 - 0.03 \mu\text{g L}^{-1}$; Table
642 2) since NPP is roughly the product of phytoplankton growth and biomass (Marchetti et al. 2009). Thus, although
643 growth rate was low, biomass was so high that NPP was also high. Furthermore, most of the primary production was
644 directly consumed by microzooplankton, which we have not observed during any other summer NES-LTER cruise,
645 suggesting the presence of *Hemiaulus* led to more efficient trophic transfer during August 2019. While conditions
646 with high NCP (i.e. low community respiration) and high grazing pressure as observed in August 2019 may seem
647 counterintuitive, they are not contradictory since grazing cannot be equated with respiration. First, much of
648 respiration is bacterial and therefore not reflected by the grazing rates (Robinson and Williams, 2005). Second, it has
649 been observed that after starvation, protozoan grazers increase their organic matter production by accumulating
650 lipids and increasing their cell size (Anderson and Menden-Deuer, 2017; Morison et al., 2020). Thus, high grazing
651 could suggest a buildup of organic matter through secondary production, which is consistent with the higher than
652 average microzooplankton biomass and would be reflected as large NCP. Third, microzooplankton can produce
653 fecal pellets (Buck and Newton, 1995), which removes carbon from the system without respiration and leads to high
654 NCP. The dominant presence, and slow growth, of large *Hemiaulus* cells within the phytoplankton community was

655 likely a main factor promoting the higher trophic transfer efficiency from phytoplankton to microzooplankton, as is
656 typical during winter (Marrec et al., 2021).

657 Interestingly, NCP and GOP values in summer 2018 were similar to those in August 2019 (Table 2, Fig. 5
658 and 8) and also much higher than during subsequent summers (2020-2022), in spite of no *Hemiaulus* being present
659 in summer 2018. Additionally, the ratio of NCP/GOP in summer of 2018 was also significantly larger than in 2020-
660 22 (Fig. 5 and 8). Remote sensing shows an elevated Chl-a patch (less concentrated than the patch in August 2019)
661 in summer 2018 west of the transect that could be the driving factor behind the high NCP and GOP values (Fig.
662 S3). The summer of 2018 was dominated by small phytoplankton similar to observations in summers of 2020 and
663 2021, although the summer of 2018 had a particularly high concentration of dinoflagellates over parts of the shelf.
664 The summer 2018 data did not show an increase in trophic transfer efficiency due to coupled microzooplankton
665 grazing and phytoplankton growth. High NCP rates in summer 2018 could be due to a variety of environmental
666 (biotic and abiotic) factors that were different from other cruises. For example, in the summer of 2018, saline waters
667 from offshore intruded much farther inshore than during most of the other summers and these high-salinity mid-
668 shelf waters were particularly productive (Mehta, 2022). Additionally, correspondence was seen between NCP and
669 dinoflagellate biomass in summer 2018, although this correlation was not as significant as that between *Hemiaulus*
670 and NCP in 2019 (Aldrett, 2021). Thus, this study shows that a change in community composition, such as the
671 *Hemiaulus* bloom in August 2019, can dramatically change the productivity rates of the ecosystem even though a
672 very different phytoplankton community structure can sometimes lead to similarly high productivity.

673 4.2 Aggregate vs Compositional Variability

674 The changes in community composition, productivity rates, and chlorophyll in August 2019 compared to the other
675 summers shed interesting light on the question of synchrony or compensation between aggregate and compositional
676 variability at the NES-LTER site (Micheli et al., 1999; Shoemaker et al., 2022). The resilience of an ecosystem may
677 be related to the compensation or synchrony between different types of variability (Lindgren et al., 2016). During
678 August 2019, the phytoplankton composition in the NES changed dramatically due to the bloom of the diatom
679 *Hemiaulus*. This change was associated with increases in Chl-a, higher productivity rates, tighter coupling between
680 microzooplankton grazing and phytoplankton growth, and increases in export efficiency. These latter terms are all
681 metrics of aggregate properties and thus this bloom event exhibited high compositional and high aggregate
682 variability compared to the ecosystem in July of 2020-22. Thus, during this event, a metric associated with
683 compositional variability (e.g., the change in phytoplankton community composition) was synchronous with metrics
684 associated with aggregate variability. However, when NCP rates are compared from the summer 2018 to summer
685 2019, the composition is still quite different (*Hemiaulus* in 2019 compared to mostly small phytoplankton in 2018)
686 and thus there is still large compositional variability but the aggregate properties in terms of NCP is similar in both
687 years, showing that sometimes compensation occurs in which the community composition changes but the aggregate
688 productivity does not. This concurrent investigation of plankton community composition and production rates within
689 a well-studied ecosystem highlights how shifts in community size distribution can greatly affect productivity.
690 However, it also shows that multiple factors change from year to year, leading to different effects.

691 4.3 Origin of Bloom

692 The *Hemiaulus* bloom was likely more widespread than what was observed in the NES-LTER 2019 summer cruise.
693 For example, satellite imagery from August 11 shows a filament of warm, high Chl-a waters oriented southwest-
694 northeast and ending in the region where *Hemiaulus* was abundant (Fig. 11a & b); the advective continuity of the
695 filament with the *Hemiaulus* patch suggests the filament may have had high *Hemiaulus* as well. Direct support for a
696 widespread bloom comes from IFCB data collected on the NOAA EcoMon Cruise (GU1902) that occurred at a
697 similar time as the August 2019 NES-LTER transect cruise. The IFCB data shows that *Hemiaulus* was present both
698 farther east as well as to the southwest of where it was observed on the LTER transect cruise and that some of the
699 points in the high chlorophyll filament observed from satellite chlorophyll contained *Hemiaulus* (Fig. 11c).

700 Backward particle trajectory analysis based on HF radar-measured sea surface velocities show that the
701 water with high *Hemiaulus* biomass during the August 2019 transect cruise could have been advected from the
702 inner-shelf around Narragansett Bay and Georges Bank rather than from the mid-shelf further south (Fig. S6). In
703 particular, coastal upwelling probably brought the inner-shelf water into the mid-shelf transect area where it was
704 observed to have high *Hemiaulus*. The salinity of the water with the high *Hemiaulus* biomass is consistent with the
705 water having originated from the shelf. The water with high amounts of *Hemiaulus* carbon was associated with
706 salinity ranging from 31.6 to 34 psu and temperatures of 22° C to 27° C (Fig. 12a & b). T-S plots of data from other

707 years (Fig. 12c) suggest that
 708 several other summers also had
 709 similarly warm, low salinity
 710 water (in particular July of 2020
 711 and especially 2022) but
 712 interestingly *Hemiaulus* were
 713 not observed on those cruises.

714 Although multiple lines
 715 of evidence suggest that the
 716 water containing the high
 717 biomass of *Hemiaulus* initially
 718 originated from the inner-shelf,
 719 *Hemiaulus* is typically found in
 720 warm, low nutrient water –
 721 characteristics that are not
 722 present on the inner-shelf, where
 723 water is instead colder and
 724 nutrient-rich. In this case, the
 725 inner-shelf water warmed as it
 726 was transported offshore and
 727 thus it reached temperatures
 728 warm enough for *Hemiaulus* to
 729 thrive by the time it reached the
 730 mid-shelf (the timing of
 731 warming is not known). But
 732 how did this inner-shelf water
 733 acquire *Hemiaulus* as it was
 734 transported offshore in August
 735 2019? One possibility is that it
 736 was seeded by the warmer low
 737 nutrient surface slope and ring
 738 waters; in particular, these slope
 739 and ring waters were observed
 740 earlier in the summer of 2019 to
 741 have a small population of
 742 *Hemiaulus* that could have
 743 served as a seed population
 744 (Oliver et al., 2021). However,
 745 there is no evidence of surface
 746 transport from slope-water to the
 747 *Hemiaulus* patch. Another
 748 possibility is that *Hemiaulus*
 749 were already present in the
 750 deeper coastal water and then
 751 thrived as the deep water was
 752 mixed upward, warmed and
 753 reached the higher light surface
 754 waters. However, the vertical
 755 distributions of *Hemiaulus* (Fig. 3) do not support this hypothesis, since a deeper population was not
 756 observed. Finally, the modeled backward particle trajectories suggesting an inner-shelf origin may be inaccurate as
 757 shelf water circulation is complex, as seen by the conflicting origins of the *Hemiaulus* water to both the east and
 758 west of the transect and an inconsistency between conclusions from the particle trajectory analysis with the high
 759 Chl-a, high temperature filament observed in the Satellite imagery (Fig S6). Thus, the reason *Hemiaulus* bloomed in
 760 2019, and not in other years, remains a topic for future research and continued speculation. Future years of the NES-
 761 LTER program may shed light on the variable effects of disturbances, such as this *Hemiaulus* bloom, as more
 762 factors that lead to high or low export in summer are determined and explored.

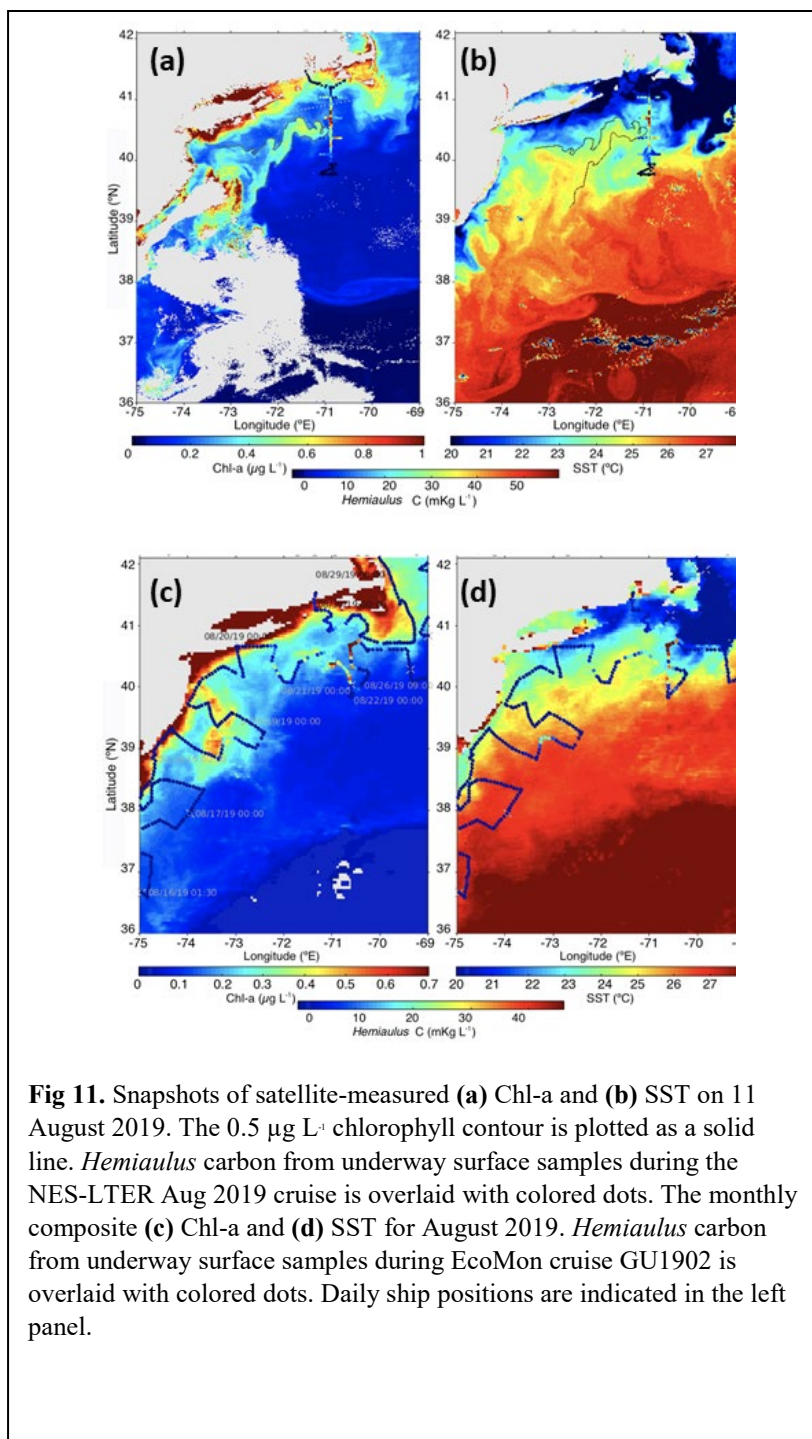


Fig 11. Snapshots of satellite-measured (a) Chl-a and (b) SST on 11 August 2019. The $0.5 \mu\text{g L}^{-1}$ chlorophyll contour is plotted as a solid line. *Hemiaulus* carbon from underway surface samples during the NES-LTER Aug 2019 cruise is overlaid with colored dots. The monthly composite (c) Chl-a and (d) SST for August 2019. *Hemiaulus* carbon from underway surface samples during EcoMon cruise GU1902 is overlaid with colored dots. Daily ship positions are indicated in the left panel.

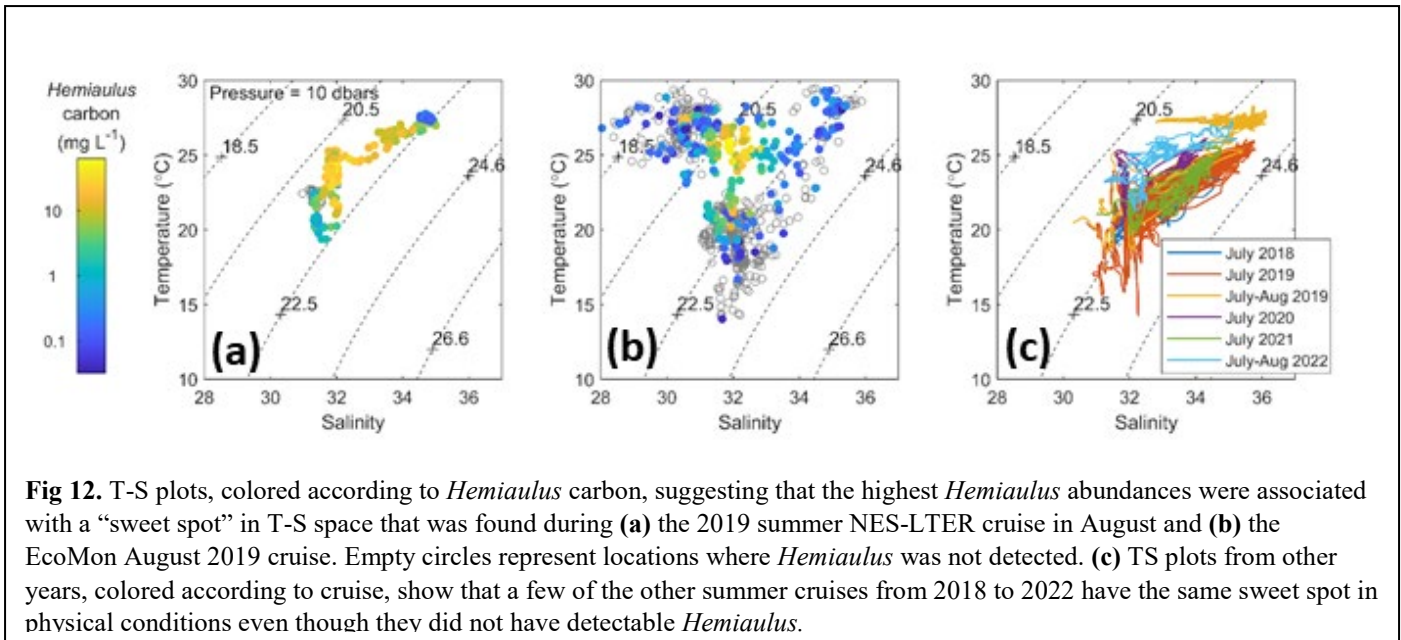


Fig 12. T-S plots, colored according to *Hemiaulus* carbon, suggesting that the highest *Hemiaulus* abundances were associated with a “sweet spot” in T-S space that was found during (a) the 2019 summer NES-LTER cruise in August and (b) the EcoMon August 2019 cruise. Empty circles represent locations where *Hemiaulus* was not detected. (c) TS plots from other years, colored according to cruise, show that a few of the other summer cruises from 2018 to 2022 have the same sweet spot in physical conditions even though they did not have detectable *Hemiaulus*.

763

764 **5 Conclusions**

765 An unusual bloom of the diatom genus *Hemiaulus* with nitrogen-fixing symbionts in the mid-shelf region of the
 766 Northeast U.S. shelf in August 2019 was observed concomitant with increases in NCP, GOP, NPP, higher export
 767 efficiency, and higher trophic transfer efficiency from phytoplankton to microzooplankton. Very tight coupling
 768 observed between kilometer-scale changes in NCP and the carbon biomass of *Hemiaulus* showed a substantial effect
 769 from the *Hemiaulus* bloom on important biogeochemical rates and stocks of the Northeast U.S. Shelf. While the
 770 source of the *Hemiaulus* on the inner-shelf remains unknown, the bloom was associated with warmer temperatures
 771 than usually observed on the shelf which may have been an important factor that facilitated the bloom when it was
 772 transported from the inner-shelf.

773 The *Hemiaulus* bloom, which was observed at a time when there were warmer sea surface temperatures
 774 especially in the outer-shelf region, was intriguing in that it led to unusually high productivity rates, increases in
 775 Chl-a concentrations, and tighter food-web coupling. While the warm SST may have contributed to the *Hemiaulus*
 776 bloom, the summer cruise of 2022 showed nearly as high water temperature as 2019 in the outer-shelf and the
 777 summers of both 2020 and 2022 had similarly high water temperatures as 2019 in the mid-shelf region. However,
 778 summers 2020 and 2022 had relatively low (i.e., average summer) productivity rates and Chl-a. So, summers 2020
 779 and 2022 had fairly similar physical conditions to that of 2019, but no significant bloom was observed, and no high-
 780 carbon export system was present. Thus, higher temperatures are not enough to explain higher productivity rates, a
 781 shift in community composition is also necessary. A mixture of the right physical conditions and community
 782 composition, like this special case of 2019, are needed for a high-carbon export system to be supported on the
 783 mid-shelf during summer.

784 With climate change, the oceans are warming at a rapid rate, and are likely moving towards warmer more
 785 stratified conditions (e.g., lower nitrate stock in surface waters) (Li et al., 2020) which may lead to less productivity
 786 and thus lower export efficiencies. However, these conditions may also lead to unusual phytoplankton composition
 787 as species distribution shifts. The results presented here show that unusual events can lead to large locally and
 788 episodically enhanced productivity and export; despite a commonly nitrate-limited ecosystem during the summer
 789 season, an intense phytoplankton bloom in summer occurred due to a symbiotic diatom-diazotroph relationship.
 790 These observations lead to further questions about how the NES ecosystem is responding to the effects of climate
 791 change such as enhanced stratification. Monitoring future disturbances and their effects will provide new insights

792 into relationships, mechanisms, and patterns of composition and productivity that may be only occasionally
793 occurring now but are likely more prevalent in the future.

794 **6 Data Availability**

795 All in situ data are available at the EDI data repository. In particular, the raw gas tracer data used for calculating
796 NCP and GOP is available at
797 <https://portal.edirepository.org/nis/mapbrowse?packageid=knb-lter-nes.6.2>. The calculated rates of NCP data is
798 accessible at <https://portal.edirepository.org/nis/mapbrowse?packageid=knb-lter-nes.7.2>
799 and <https://portal.edirepository.org/nis/mapbrowse?packageid=knb-lter-nes.15.2>. NPP data is available at
800 <https://portal.edirepository.org/nis/metadataviewer?packageid=knb-lter-nes.16.4>. Grazing rate data is available at
801 <https://portal.edirepository.org/nis/mapbrowse?packageid=knb-lter-nes.5.1>. Chlorophyll data is available at
802 <https://portal.edirepository.org/nis/mapbrowse?packageid=knb-lter-nes.8.1>. IFCB data is available at
803 <https://portal.edirepository.org/nis/mapbrowse?packageid=knb-lter-nes.9.1> and on the IFCB dashboard
804 at https://ifcb-data.whoi.edu/timeline?dataset=NESLTER_transect and [https://ifcb-](https://ifcb-data.whoi.edu/timeline?dataset=NESLTER_broadscale)
805 [data.whoi.edu/timeline?dataset=NESLTER_broadscale](https://ifcb-data.whoi.edu/timeline?dataset=NESLTER_broadscale). .
806

807 The MODIS SST and chlorophyll snapshot data were produced by NASA Goddard Space Flight Center, Ocean
808 Ecology Laboratory, Ocean Biology Processing Group, and the data are publicly available at
809 <https://oceancolor.gsfc.nasa.gov/>. The 8-day composite data were retrieved from the public-accessible University of
810 Delaware ERDDAP server (<https://basin.ceoe.udel.edu/erddap/index.html>) maintained by the Ocean Exploration,
811 Remote Sensing and Biogeography Laboratory led by Dr. Matthew Oliver at University of Delaware. The HF radar-
812 measured sea surface velocity data in July-August 2019 was obtained from the public-accessible Rutgers University
813 Center for Ocean Observing Leadership ERDDAP server (<http://hfr.marine.rutgers.edu/erddap/griddap/>).

814 **Author Contribution**

815 SAC, RHRS, ZOS, and DA measured and calculated rates of productivity from gas tracers. SMD and PM measured
816 grazing rates. TAR and DNF measured and calculated rates of net primary productivity from bottle incubations.
817 HMS, ETC and EEP imaged and quantified phytoplankton abundances. DJM and WGZ analyzed remote sensing
818 data. Everyone participated in study design. SAC and RHRS prepared the manuscript with contributions from all co-
819 authors.

820 **Competing Interests**

821 The authors declare that they have no conflict of interest.

822 **Acknowledgements**

823 This work was funded by the National Science Foundation (LTER-1655686, OCE-1657489, OCE-1657803, OCE-
824 2227425) and the Simons Foundation (561126 to HMS). S. A. Castillo Cieza was supported by the Clara Boothe
825 Luce Fellowship program at Wellesley College. We are thankful for the scientific input, discussions and help from
826 the entire NES-LTER science team. We are grateful to the Captain and crew of the *R/V Endeavor*. We thank Harvey
827 Walsh, Jerome Prezioso, Audy Peoples and Tamara Holzwarth-Davis for their cooperation and enthusiasm for IFCB
828 operations on NOAA survey cruises. We recognize the contributions of Kevin Cahill (WHOI), who ran some of the
829 samples for triple oxygen isotope measurement, Elizabeth Lambert (Wellesley College) and Helene Alt (Wellesley
830 College) who helped collect some of the EIMS data, and Danielle Aldrett (Wellesley College) for doing some initial
831 analysis on connections between the IFCB and NCP data. We thank NES-LTER data manager Stace Beaulieu and
832 Kate Morkeski (WHOI) for their help in data management. We thank URI-GSO undergraduate and graduate
833 students and postdocs who helped collect samples and conduct experiments to obtain chl-*a* concentrations, and
834 phytoplankton growth and microzooplankton grazing rates. We thank Sam Setta for pointing out *Richelia* in IFCB

835 images during the 2019 summer cruise. DJM gratefully acknowledges NSF support of the SPIROPA program, and
836 technical assistance by Olga Kosnyrev in satellite data analysis and visualization.

837 References

- 838 Aldrett, D.: Understanding the relationship between photosynthetic organisms and oceanic productivity
839 in the Northeast U.S. Shelf, undergraduate thesis, Chemistry, Wellesley College, Wellesley, MA
840 USA, 58 pp., 2021.
- 841 Anderson, S. R. and Menden-Deuer, S.: Growth, Grazing, and Starvation Survival in Three
842 Heterotrophic Dinoflagellate Species, *Journal of Eukaryotic Microbiology*, 64, 213-225,
843 <https://doi.org/10.1111/jeu.12353>, 2017.
- 844 Armbrust, E. V.: The life of diatoms in the world's oceans, *Nature*, 459, 185-192, 10.1038/nature08057,
845 2009.
- 846 Barkan, E. and Luz, B.: The relationships among the three stable isotopes of oxygen in air, seawater and
847 marine photosynthesis, *Rapid Communications in Mass Spectrometry*, 25, 2367-2369,
848 10.1002/rcm.5125, 2011.
- 849 Boyd, P. W., Claustre, H., Levy, M., Siegel, D. A., and Weber, T.: Multi-faceted particle pumps drive
850 carbon sequestration in the ocean, *Nature*, 568, 327-335, 10.1038/s41586-019-1098-2, 2019.
- 851 Brownlee, E. F., Olson, R. J., and Sosik, H. M.: Microzooplankton community structure investigated
852 with imaging flow cytometry and automated live-cell staining, *Marine Ecology Progress Series*, 550,
853 65-81, 10.3354/meps11687, 2016.
- 854 Buck, K. R. and Newton, J.: FECAL PELLET FLUX IN DABOB BAY DURING A DIATOM BLOOM
855 - CONTRIBUTION OF MICROZOOPLANKTON, *Limnology and Oceanography*, 40, 306-315,
856 10.4319/lo.1995.40.2.0306, 1995.
- 857 Carpenter, E. J., Montoya, J. P., Burns, J., Mulholland, M. R., Subramaniam, A., and Capone, D. G.:
858 Extensive bloom of a N-2-fixing diatom/cyanobacterial association in the tropical Atlantic Ocean,
859 *Marine Ecology Progress Series*, 185, 273-283, 10.3354/meps185273, 1999.
- 860 Cassar, N., Barnett, B. A., Bender, M. L., Kaiser, J., Hamme, R. C., and Tilbrook, B.: Continuous High-
861 Frequency Dissolved O-2/Ar Measurements by Equilibrator Inlet Mass Spectrometry, *Analytical*
862 *Chemistry*, 81, 1855-1864, 2009.
- 863 Catlett, D., Peacock, E. E., Crockford, E. T., Futrelle, J., Batchelder, S., Stevens, B. L. F., Gast, R.,
864 Zhang, W. G., and Sosik, H. M.: Temperature dependence of parasitoid infection and abundance of a
865 diatom revealed by automated imaging and classification, *Proceedings of the National Academy of*
866 *Science, U.S.A.*, 120, e2303356120, doi:10.1073/pnas.2303356120, 2023.
- 867 Cetinic, I., Poulton, N., and Slade, W. H.: Characterizing the phytoplankton soup: pump and plumbing
868 effects on the particle assemblage in underway optical seawater systems, *Optics Express*, 24, 20703-
869 20715, 10.1364/oe.24.020703, 2016.
- 870 Chen, B. Z.: Assessing the accuracy of the "two-point" dilution technique, *Limnol. Oceanogr. Meth.*, 13,
871 521-526, 10.1002/lom3.10044, 2015.
- 872 Chen, Z. M., Kwon, Y. O., Chen, K., Fratantoni, P., Gawarkiewicz, G., and Joyce, T. M.: Long-Term
873 SST Variability on the Northwest Atlantic Continental Shelf and Slope, *Geophysical Research*
874 *Letters*, 47, 10.1029/2019gl085455, 2020.
- 875 Coplen, T. B.: Reporting of stable hydrogen, carbon, and oxygen isotopic abundances - (Technical
876 report), *Geothermics*, 24, 708-712, 1995.
- 877 de Boyer Montegut, C., Madec, G., Fischer, A. S., Lazar, A., and Iudicone, D.: Mixed layer depth over
878 the global ocean: An examination of profile data and a profile-based climatology, *J. Geophys. Res.-*
879 *Oceans*, 109, 10.1029/2004jc002378, 2004.
- 880 Dore, J. E., Letelier, R. M., Church, M. J., Lukas, R., and Karl, D. M.: Summer phytoplankton blooms in
881 the oligotrophic North Pacific Subtropical Gyre: Historical perspective and recent observations,
882 *Progress in Oceanography*, 76, 2-38, 10.1016/j.pocean.2007.10.002, 2008.

883 Dugdale, R. C. and Goering, J. J.: Uptake of new and regenerated forms of nitrogen in primary
884 productivity., *Limnology and Oceanography*, 12, 196-206, 1967.

885 Emerson, S.: Annual net community production and the biological carbon flux in the ocean, *Global*
886 *Biogeochemical Cycles*, 28, 14-28, 10.1002/2013gb004680, 2014.

887 Field, C. B., Behrenfeld, M. J., Randerson, J. T., and Falkowski, P.: Primary production of the biosphere:
888 Integrating terrestrial and oceanic components, *Science*, 281, 237-240,
889 10.1126/science.281.5374.237, 1998.

890 Foster, R. A. and Zehr, J. P.: Characterization of diatom-cyanobacteria symbioses on the basis of *nifH*,
891 *hetR* and 16S rRNA sequences, *Environ. Microbiol.*, 8, 1913-1925, 10.1111/j.1462-
892 2920.2006.01068.x, 2006.

893 Foster, R. A. and Zehr, J. P.: Diversity, Genomics, and Distribution of Phytoplankton- Cyanobacterium
894 Single-Cell Symbiotic Associations, in: *Annual Review of Microbiology*, Vol 73, edited by:
895 Gottesman, S., *Annual Review of Microbiology*, 435-456, 10.1146/annurev-micro-090817-062650,
896 2019.

897 Friedlingstein, P., Jones, M. W., O'Sullivan, M., Andrew, R. M., Bakker, D. C. E., Hauck, J., Le Quere,
898 C., Peters, G. P., Peters, W., Pongratz, J., Sitch, S., Canadell, J. G., Ciais, P., Jackson, R. B., Alin, S.
899 R., Anthoni, P., Bates, N. R., Becker, M., Bellouin, N., Bopp, L., Chau, T. T. T., Chevallier, F.,
900 Chini, L. P., Cronin, M., Currie, K. I., Decharme, B., Djeutchouang, L. M., Dou, X. Y., Evans, W.,
901 Feely, R. A., Feng, L., Gasser, T., Gilfillan, D., Gkritzalis, T., Grassi, G., Gregor, L., Gruber, N.,
902 Gurses, O., Harris, I., Houghton, R. A., Hurtt, G. C., Iida, Y., Ilyina, T., Lujikx, I. T., Jain, A., Jones,
903 S. D., Kato, E., Kennedy, D., Goldewijk, K. K., Knauer, J., Korsbakken, J. I., Kortzinger, A.,
904 Landschutzer, P., Lauvset, S. K., Lefevre, N., Lienert, S., Liu, J. J., Marland, G., McGuire, P. C.,
905 Melton, J. R., Munro, D. R., Nabel, J., Nakaoka, S. I., Niwa, Y., Ono, T., Pierrot, D., Poulter, B.,
906 Rehder, G., Resplandy, L., Robertson, E., Rodenbeck, C., Rosan, T. M., Schwinger, J.,
907 Schwingshackl, C., Seferian, R., Sutton, A. J., Sweeney, C., Tanhua, T., Tans, P. P., Tian, H. Q.,
908 Tilbrook, B., Tubiello, F., van der Werf, G. R., Vuichard, N., Wada, C., Wanninkhof, R., Watson, A.
909 J., Willis, D., Wiltshire, A. J., Yuan, W. P., Yue, C., Yue, X., Zaehle, S., and Zeng, J. Y.: *Global*
910 *Carbon Budget 2021*, *Earth System Science Data*, 14, 1917-2005, 10.5194/essd-14-1917-2022, 2022.

911 Garcia, H. E. and Gordon, L. I.: Oxygen solubility in water: better fitting equations, *Limnology and*
912 *Oceanography*, 37, 1307-1312, 1992.

913 Gaysina, L. A., Saraf, A., and Singh, P.: Chapter 1 - Cyanobacteria in Diverse Habitats, in:
914 *Cyanobacteria*, edited by: Mishra, A. K., Tiwari, D. N., and Rai, A. N., Academic Press, 1-28,
915 <https://doi.org/10.1016/B978-0-12-814667-5.00001-5>, 2019.

916 Grosse, J., Bombar, D., Hai, N. D., Lam, N. N., and Voss, M.: The Mekong River plume fuels nitrogen
917 fixation and determines phytoplankton species distribution in the South China Sea during low- and
918 high-discharge season, *Limnology and Oceanography*, 55, 1668-1680, 10.4319/lo.2010.55.4.1668,
919 2010.

920 Hama, T., Miyazaki, T., Ogawa, Y., Iwakuma, T., Takahashi, M., Otsuki, A., and Ichimura, S.:
921 Measurement of photosynthetic production of a marine phytoplankton population using a stable ¹³C
922 isotope, *Marine Biology*, 73, 31-36, 10.1007/BF00396282, 1983.

923 Hamme, R. C. and Emerson, S.: The solubility of neon, nitrogen and argon in distilled water and
924 seawater, *Deep Sea Research I*, 51, 1517-1528, 2004.

925 Hendricks, M. B., Bender, M. L., and Barnett, B. A.: Net and gross O₂ production in the Southern
926 Ocean from measurements of biological O₂ saturation and its triple isotope composition, *Deep-Sea*
927 *Res. Part I-Oceanogr. Res. Pap.*, 51, 1541-1561, 2004.

928 Jakobsen, H. H. and Markager, S.: Carbon to chlorophyll ratio for phytoplankton in temperate coastal
929 waters: Seasonal patterns and relationship to nutrients. , *Limnology and Oceanography*, 61, 1853-
930 1868, doi:10.1002/lno.10338, 2016.

931 Jin, X., Gruber, N., Dunne, J. P., Sarmiento, J. L., and Armstrong, R. A.: Diagnosing the contribution of
932 phytoplankton functional groups to the production and export of particulate organic carbon, CaCO₃,

933 and opal from global nutrient and alkalinity distributions, *Global Biogeochemical Cycles*, 20,
934 10.1029/2005gb002532, 2006.

935 Juranek, L. W. and Quay, P. D.: In vitro and in situ gross primary and net community production in the
936 North Pacific Subtropical Gyre using labeled and natural abundance isotopes of dissolved O-2,
937 *Global Biogeochemical Cycles*, 19, doi:10.1029/2004GB002384, 2005.

938 Juranek, L. W. and Quay, P. D.: Using Triple Isotopes of Dissolved Oxygen to Evaluate Global Marine
939 Productivity, in: *Annual Review of Marine Science*, Vol 5, edited by: Carlson, C. A., and
940 Giovannoni, S. J., *Annual Review of Marine Science*, Annual Reviews, Palo Alto, 503-524,
941 10.1146/annurev-marine-121211-172430, 2013.

942 Juranek, L. W., Hamme, R. C., Kaiser, J., Wanninkhof, R., and Quay, P. D.: Evidence of O-2
943 consumption in underway seawater lines: Implications for air-sea O-2 and CO2 fluxes, *Geophysical
944 Research Letters*, 37, doi:10.1029/2009GL040423, 2010.

945 Kalnay, E., Kanamitsu, M., Kistler, R., Collins, W., Deaven, D., Gandin, L., Iredell, M., Saha, S., White,
946 G., Woollen, J., Zhu, Y., Chelliah, M., Ebisuzaki, W., Higgins, W., Janowiak, J., Mo, K. C.,
947 Ropelewski, C., Wang, J., Leetmaa, A., Reynolds, R., Jenne, R., and Joseph, D.: The NCEP/NCAR
948 40-year reanalysis project, *Bulletin of the American Meteorological Society*, 77, 437-471,
949 10.1175/1520-0477(1996)077<0437:TNYRP>2.0.CO;2, 1996.

950 Kara, A. B., Rochford, P. A., and Hurlburt, H. E.: An optimal definition for ocean mixed layer depth, *J.
951 Geophys. Res.-Oceans*, 105, 16803-16821, 10.1029/2000jc900072, 2000.

952 Karl, D. M., Church, M. J., Dore, J. E., Letelier, R. M., and Mahaffey, C.: Predictable and efficient
953 carbon sequestration in the North Pacific Ocean supported by symbiotic nitrogen fixation,
954 *Proceedings of the National Academy of Sciences of the United States of America*, 109, 1842-1849,
955 10.1073/pnas.1120312109, 2012.

956 Karmalkar, A. V. and Horton, R. M.: Drivers of exceptional coastal warming in the northeastern United
957 States, *Nature Climate Change*, 11, 854+, 10.1038/s41558-021-01159-7, 2021.

958 Kemp, A. E. S. and Villareal, T. A.: High diatom production and export in stratified waters - A potential
959 negative feedback to global warming, *Progress in Oceanography*, 119, 4-23,
960 10.1016/j.pocean.2013.06.004, 2013.

961 Kemp, A. E. S. and Villareal, T. A.: The case of the diatoms and the muddled mandalas: Time to
962 recognize diatom adaptations to stratified waters, *Progress in Oceanography*, 167, 138-149,
963 10.1016/j.pocean.2018.08.002, 2018.

964 Kistler, R., Kalnay, E., Collins, W., Saha, S., White, G., Woollen, J., Chelliah, M., Ebisuzaki, W.,
965 Kanamitsu, M., Kousky, V., van den Dool, H., Jenne, R., and Fiorino, M.: The NCEP-NCAR 50-year
966 reanalysis: Monthly means CD-ROM and documentation, *Bulletin of the American Meteorological
967 Society*, 82, 247-267, 2001.

968 Landry, M. R. and Calbet, A.: Microzooplankton production in the oceans, *ICES J. Mar. Sci.*, 61, 501-
969 507, 10.1016/j.icesjms.2004.03.011, 2004.

970 Landry, M. R., Brown, S. L., Neveux, J., Dupouy, C., J., B., Christensen, S., and Bidigare, R. R.:
971 Phytoplankton growth and microzooplankton grazing in high-nutrient, low-chlorophyll waters of the
972 equatorial Pacific: Community and taxon-specific rate assessments from pigment and flow cytometric
973 analyses, *JGR Oceans*, 108, <https://doi.org/10.1029/2000JC000744>, 2003.

974 Landry, M. R., Brown, S. L., Rii, Y. M., Selph, K. E., Bidigare, R. R., Yang, E. J., and Simmons, M. P.:
975 Depth-stratified phytoplankton dynamics in Cyclone Opal, a subtropical mesoscale eddy, *Deep-Sea
976 Research Part II-Topical Studies in Oceanography*, 55, 1348-1359, 10.1016/j.dsr2.2008.02.001, 2008.

977 Lange, M. and van Sebille, E.: Parcels v0.9: prototyping a Lagrangian ocean analysis framework for the
978 petascale age, *Geosci. Model Dev.*, 10, 4175-4186, 10.5194/gmd-10-4175-2017, 2017.

979 Li, G. C., Cheng, L. J., Zhu, J., Trenberth, K. E., Mann, M. E., and Abraham, J. P.: Increasing ocean
980 stratification over the past half-century, *Nature Climate Change*, 10, 1116-U1176, 10.1038/s41558-
981 020-00918-2, 2020.

982 Li, Y., Fratantoni, P. S., Chen, C. S., Hare, J. A., Sun, Y. F., Beardsley, R. C., and Ji, R. B.: Spatio-
983 temporal patterns of stratification on the Northwest Atlantic shelf, *Progress in Oceanography*, 134,
984 123-137, 10.1016/j.pocean.2015.01.003, 2015.

985 Lindegren, M., Checkley, D. M., Ohman, M. D., Koslow, J. A., and Goericke, R.: Resilience and
986 stability of a pelagic marine ecosystem, *Proceedings of the Royal Society B-Biological Sciences*, 283,
987 10.1098/rspb.2015.1931, 2016.

988 Lomas, M. W., Moran, S. B., Casey, J. R., Bell, D. W., Tiahlo, M., Whitefield, J., Kelly, R. P., Mathis, J.
989 T., and Cokelet, E. D.: Spatial and seasonal variability of primary production on the Eastern Bering
990 Sea shelf, *Deep-Sea Research Part II-Topical Studies in Oceanography*, 65-70, 126-140,
991 10.1016/j.dsr2.2012.02.010, 2012.

992 Malviya, S., Scalco, E., Audic, S., Vincenta, F., Veluchamy, A., Poulain, J., Wincker, P., Iudicone, D.,
993 de Vargas, C., Bittner, L., Zingone, A., and Bowler, C.: Insights into global diatom distribution and
994 diversity in the world's ocean, *Proceedings of the National Academy of Sciences of the United States*
995 *of America*, 113, E1516-E1525, 10.1073/pnas.1509523113, 2016.

996 Manning, C., Stanley, R. H. R., and Lott III, D. E.: Continuous Measurements of Dissolved Ne, Ar, Kr,
997 and Xe Ratios with a Field-deployable Gas Equilibration Mass Spectrometer, *Analytical Chemistry*,
998 88, 3040-3048, doi: 10.1021/acs.analchem.5b03102, 2016.

999 Manning, C. C., Howard, E. M., Nicholson, D. P., Ji, B. Y., Sandwith, Z. O., and Stanley, R. H. R.:
1000 Revising estimates of aquatic gross oxygen production by the triple oxygen isotope method to
1001 incorporate the local isotopic composition of water., *Geophysical Research Letters*, 44,
1002 10.1002/2017GL074375, 2017a.

1003 Manning, C. C., Stanley, R. H. R., Nicholson, D. P., Smith, J. M., Pennington, J. T., Fewings, M. R.,
1004 Squibb, M. E., and Chavez, F. P.: Impact of recently upwelled water on productivity investigated
1005 using in situ and incubation-based methods in Monterey Bay, *J. Geophys. Res.-Oceans*, 122, 1901-
1006 1926, 10.1002/2016JC012306., 2017b.

1007 Margalef, R.: Life-forms of phytoplankton as survival alternatives in an unstable environment,
1008 *Oceanologica Acta*, 1, 493-509, 1978.

1009 Marrec, P., McNair, H., Franze, G., Morison, F., Strock, J. P., and Menden-Deuer, S.: Seasonal
1010 variability in planktonic food web structure and function of the Northeast US Shelf, *Limnology and*
1011 *Oceanography*, 66, 1440-1458, 10.1002/lno.11696, 2021.

1012 Mehta, A.: Spatial and Temporal Heterogeneity in Net Community Production in the Crossshelf
1013 Direction of the Atlantic Northeastern Shelf, undergraduate thesis, Chemistry, Wellesley College,
1014 Wellesley, MA USA, 86 pp., 2022.

1015 Menden-Deuer, S. and Lessard, E.: Menden-Deuer S, Lessard EJ.. Carbon to volume relationships for
1016 dinoflagellates, diatoms, and other protist plankton. *Limnol Oceanogr* 45: 569-579, *Limnology and*
1017 *oceanography*, 45, 569-579, 10.4319/lo.2000.45.3.0569, 2000.

1018 Micheli, F., Cottingham, K. L., Bascompte, J., Bjornstad, O. N., Eckert, G. L., Fischer, J. M., Keitt, T.
1019 H., Kendall, B. E., Klug, J. L., and Rusak, J. A.: The dual nature of community variability, *Oikos*, 85,
1020 161-169, 10.2307/3546802, 1999.

1021 Millero, F. J. and Poisson, A.: International One-Atmosphere Equation of State of Seawater, *Deep-Sea*
1022 *Research Part a-Oceanographic Research Papers*, 28, 625-629, 1981.

1023 Moberg, E. A. and Sosik, H. M.: Distance maps to estimate cell volume from two-dimensional plankton
1024 images, *Limnol. Oceanogr. Meth.*, 10, 278-288, 10.4319/lom.2012.10.278, 2012.

1025 Morison, F., Franzè, G., Harvey, E., and Menden-Deuer, S.: Light fluctuations are key in modulating
1026 plankton trophic dynamics and their impact on primary production, *Limnology and Oceanography*
1027 *Letters*, 5, 346-353, <https://doi.org/10.1002/lol2.10156>, 2020.

1028 Mouw, C. B. and Yoder, J. A.: Primary production calculations in the Mid-Atlantic Bight, including
1029 effects of phytoplankton community size structure, *Limnology and Oceanography*, 50, 1232-1243,
1030 2005.

1031 O'Reilly, J. E. and Zetlin, C.: Seasonal, horizontal and vertical distribution of phytoplankton chlorophyll
1032 a in the Northeast U.S. Continental Shelf Ecosystem., 1998.

1033 Oliver, H., Zhang, W. G., Archibald, K. M., Hirzel, A. J., Smith, W. O., Sosik, H. M., Stanley, R. H. R.,
1034 and McGillicuddy, D. J.: Ephemeral Surface Chlorophyll Enhancement at the New England Shelf
1035 Break Driven by Ekman Restratification, *J. Geophys. Res.-Oceans*, 127, 10.1029/2021jc017715,
1036 2022.

1037 Oliver, H., Zhang, W. F., Smith, W. O., Alatalo, P., Chappell, P. D., Hirzel, A. J., Selden, C. R., Sosik,
1038 H. M., Stanley, R. H. R., Zhu, Y. F., and McGillicuddy, D. J.: Diatom Hotspots Driven by Western
1039 Boundary Current Instability, *Geophysical Research Letters*, 48, 10.1029/2020gl091943, 2021.

1040 Olson, R. J. and Sosik, H. M.: A submersible imaging-in-flow instrument to analyze nano-and
1041 microplankton: Imaging FlowCytobot, *Limnol. Oceanogr. Meth.*, 5, 195-203,
1042 10.4319/lom.2007.5.195, 2007.

1043 Palevsky, H. I., Quay, P. D., Lockwood, D. E., and Nicholson, D. P.: The annual cycle of gross primary
1044 product ion, net community production, and export efficiency across the North Pacific Ocean, *Global
1045 Biogeochem. Cycles*, 30, 361-380, 10.1002/2015GB005318, 2016.

1046 Parsons, T. R., Maita, Y., and Lalli, C. M.: *A Manual of Chemical & Biological Methods for Seawater
1047 Analysis*, Pergamon, <https://doi.org/10.1016/C2009-0-07774-5>, 1984.

1048 Prokopenko, M. G., Pauluis, O. M., Granger, J., and Yeung, L. Y.: Exact evaluation of gross
1049 photosynthetic production from the oxygen triple-isotope composition of O(2): Implications for the
1050 net-to-gross primary production ratios, *Geophysical Research Letters*, 38,
1051 L1460310.1029/2011gl047652, 2011.

1052 Puigcorbe, V., Benitez-Nelson, C. R., Masque, P., Verdeny, E., White, A. E., Popp, B. N., Prahl, F. G.,
1053 and Lam, P. J.: Small phytoplankton drive high summertime carbon and nutrient export in the Gulf of
1054 California and Eastern Tropical North Pacific, *Global Biogeochemical Cycles*, 29, 1309-1332,
1055 10.1002/2015gb005134, 2015.

1056 Pyle, A. E., Johnson, A. M., and Villareal, T. A.: Isolation, growth, and nitrogen fixation rates of the
1057 *Hemiaulus-Richelina* (diatom-cyanobacterium) symbiosis in culture, *PeerJ*, 8, 10.7717/peerj.10115,
1058 2020.

1059 Reuer, M. K., Barnett, B. A., Bender, M. L., Falkowski, P. G., and Hendricks, M. B.: New estimates of
1060 Southern Ocean biological production rates from O-2/Ar ratios and the triple isotope composition of
1061 O-2, *Deep-Sea Res. Part I-Oceanogr. Res. Pap.*, 54, 951-974, 2007.

1062 Robinson, C. and Williams, P. J. I. B.: 147Respiration and its measurement in surface marine waters,
1063 10.1093/acprof:oso/9780198527084.003.0009, 2005.

1064 Russakovsky, O., Deng, J., Su, H., Krause, J., Satheesh, S., Ma, S., Huang, Z. H., Karpathy, A., Khosla,
1065 A., Bernstein, M., Berg, A. C., and Fei-Fei, L.: ImageNet Large Scale Visual Recognition Challenge,
1066 *International Journal of Computer Vision*, 115, 211-252, 10.1007/s11263-015-0816-y, 2015.

1067 Schmoker, C., Hernandez-Leon, S., and Calbet, A.: Microzooplankton grazing in the oceans: impacts,
1068 data variability, knowledge gaps and future directions, *Journal of Plankton Research*, 35, 691-706,
1069 10.1093/plankt/fbt023, 2013.

1070 Shearman, R. K. and Lentz, S. J.: Long-Term Sea Surface Temperature Variability along the US East
1071 Coast, *J. Phys. Oceanogr.*, 40, 1004-1017, 10.1175/2009jpo4300.1, 2010.

1072 Shoemaker, L. G., Hallett, L. M., Zhao, L., Reuman, D. C., Wang, S. P., Cottingham, K. L., Hobbs, R.
1073 J., Castorani, M. C. N., Downing, A. L., Dudley, J. C., Fey, S. B., Gherardi, L. A., Lany, N.,
1074 Portales-Reyes, C., Rypel, A. L., Sheppard, L. W., Walter, J. A., and Suding, K. N.: The long and the
1075 short of it: Mechanisms of synchronous and compensatory dynamics across temporal scales, *Ecology*,
1076 103, 10.1002/ecy.3650, 2022.

1077 Spitzer, S.: An Analysis of Diatom Growth Rate and the Implications for the Biodiesel Industry,
1078 *Occum's Razor*, 5, 2015.

1079 Stanley, R. H. R., Sandwith, Z. O., and Williams, W. J.: Rates of summertime biological productivity in
1080 the Beaufort Gyre: A comparison between the low and record-low ice conditions of August 2011 and
1081 2012, *Journal of Marine Systems*, 147, 29-44, 2015.

1082 Stanley, R. H. R., Jenkins, W. J., Doney, S. C., and Lott III, D. E.: Noble Gas Constraints on Air-Sea
1083 Gas Exchange and Bubble Fluxes, *Journal of Geophysical Research - Oceans*, 114,
1084 doi:10.1029/2009JC005396, 2009.

1085 Stanley, R. H. R., Kirkpatrick, J. B., Barnett, B., Cassar, N., and Bender, M. L.: Net community
1086 production and gross production rates in the Western Equatorial Pacific, *Global Biogeochemical*
1087 *Cycles*, 24, GB4001, doi:4010.1029/2009GB003651, 2010.

1088 Subramaniam, A., Yager, P. L., Carpenter, E. J., Mahaffey, C., Bjorkman, K., Cooley, S., Kustka, A. B.,
1089 Montoya, J. P., Sanudo-Wilhelmy, S. A., Shipe, R., and Capone, D. G.: Amazon River enhances
1090 diazotrophy and carbon sequestration in the tropical North Atlantic Ocean, *Proceedings of the*
1091 *National Academy of Sciences of the United States of America*, 105, 10460-10465,
1092 10.1073/pnas.0710279105, 2008.

1093 Szegedy, C., Vanhoucke, V., Ioffe, S., Shlens, J., and Wojna, Z.: Rethinking the Inception Architecture
1094 for Computer Vision, 2016 IEEE Conference on Computer Vision and Pattern Recognition (CVPR),
1095 27-30 June 2016, 2818-2826, 10.1109/CVPR.2016.308,

1096 Tang, W. Y., Cerdan-Garcia, E., Berthelot, H., Polyviou, D., Wang, S. V., Baylay, A., Whitby, H.,
1097 Planquette, H., Mowlem, M., Robidart, J., and Cassar, N.: New insights into the distributions of
1098 nitrogen fixation and diazotrophs revealed by high-resolution sensing and sampling methods, *Isme J.*,
1099 14, 2514-2526, 10.1038/s41396-020-0703-6, 2020.

1100 Teeter, L., Hamme, R. C., Ianson, D., and Bianucci, L.: Accurate estimation of net community
1101 production from O₂/Ar measurements, *Global Biogeochem. Cycles*, 32, 10.1029/2017GB005874,
1102 2018.

1103 Townsend, D. W., Thomas, A. C., Mayer, L. M., Thomas, A. J., and Quinlan, J. A.: Oceanography of the
1104 Northwest Atlantic continental shelf, in: *The Sea*, edited by: Robinson, A. R., and Brink, K. H.,
1105 Harvard University Press, 119-167, 2006.

1106 Twining, B. S., Nodder, S. D., King, A. L., Hutchins, D. A., LeClerc, G. R., DeBruyn, J. M., Maas, E.
1107 W., Vogt, S., Wilhelm, S. W., and Boyd, P. W.: Differential remineralization of major and trace
1108 elements in sinking diatoms, *Limnology and Oceanography*, 59, 689-704, 10.4319/lo.2014.59.3.0689,
1109 2014.

1110 Villareal, T. A.: Laboratory culture and preliminary characterization of the nitrogen-fixing *Rhizosolenia*-
1111 *Richelia* symbiosis, *Marine Ecology*, 11, 117-132, 1990.

1112 Villareal, T. A., Adornato, L., Wilson, C., and Schoenbaechler, C. A.: Summer blooms of diatom-
1113 diazotroph assemblages and surface chlorophyll in the North Pacific gyre: A disconnect, *J. Geophys.*
1114 *Res.-Oceans*, 116, 10.1029/2010jc006268, 2011.

1115 Wang, S., Tang, W. Y., Delage, E., Gifford, S., Whitby, H., Gonzalez, A. G., Eveillard, D., Planquette,
1116 H., and Cassar, N.: Investigating the microbial ecology of coastal hotspots of marine nitrogen fixation
1117 in the western North Atlantic, *Scientific Reports*, 11, 10.1038/s41598-021-84969-1, 2021.

1118 Yoder, J. A., Schollaert, S. E., and O'Reilly, J. E.: Climatological phytoplankton chlorophyll and sea
1119 surface temperature patterns in continental shelf and slope waters off the northeast US coast,
1120 *Limnology and Oceanography*, 47, 672-682, 2002.

1121 Zhang, W. F., Alatalo, P., Crockford, T., Hirzel, A. J., Meyer, M. G., Oliver, H., Peacock, E., Petitpas,
1122 C. M., Sandwith, Z., Smith, W. O., Sosik, H. M., Stanley, R. H. R., Stevens, B. L. F., Turner, J. T.,
1123 and McGillicuddy, D. J.: Cross-shelf exchange associated with a shelf-water streamer at the Mid-
1124 Atlantic Bight shelf edge, *Progress in Oceanography*, 210, 10.1016/j.pocean.2022.102931, 2023.

1125